

MIT Open Access Articles

*Maximal spontaneous photon emission
and energy loss from free electrons*

The MIT Faculty has made this article openly available. **Please share** how this access benefits you. Your story matters.

Citation: Yang, Yi, et al. "Maximal Spontaneous Photon Emission and Energy Loss from Free Electrons." *Nature Physics* 14, 9 (July 16, 2018): 894–899. © 2018 The Authors

As Published: <http://dx.doi.org/10.1038/S41567-018-0180-2>

Publisher: Springer Nature America, Inc

Persistent URL: <https://hdl.handle.net/1721.1/124634>

Version: Author's final manuscript: final author's manuscript post peer review, without publisher's formatting or copy editing

Terms of Use: Article is made available in accordance with the publisher's policy and may be subject to US copyright law. Please refer to the publisher's site for terms of use.



Maximal spontaneous photon emission and energy loss from free electrons

Yi Yang^{1*}, Aviram Massuda¹, Charles Roques-Carmes¹, Steven E. Kooi², Thomas Christensen¹, Steven G. Johnson¹, John D. Joannopoulos^{1,2}, Owen D. Miller^{3*}, Owen D. Miller^{3*}, Ido Kaminer^{1,4*} and Marin Soljačić¹

Free-electron radiation such as Cerenkov¹, Smith–Purcell² and transition radiation^{3,4} can be greatly affected by structured optical environments, as has been demonstrated in a variety of polaritonic^{5,6}, photonic-crystal⁷ and metamaterial^{8–10} systems. However, the amount of radiation that can ultimately be extracted from free electrons near an arbitrary material structure has remained elusive. Here we derive a fundamental upper limit to the spontaneous photon emission and energy loss of free electrons, regardless of geometry, which illuminates the effects of material properties and electron velocities. We obtain experimental evidence for our theory with quantitative measurements of Smith–Purcell radiation. Our framework allows us to make two predictions. One is a new regime of radiation operation—at subwavelength separations, slower (non-relativistic) electrons can achieve stronger radiation than fast (relativistic) electrons. The other is a divergence of the emission probability in the limit of lossless materials. We further reveal that such divergences can be approached by coupling free electrons to photonic bound states in the continuum^{11–13}. Our findings suggest that compact and efficient free-electron radiation sources from microwaves to the soft X-ray regime may be achievable without requiring ultrahigh accelerating voltages.

The Smith–Purcell effect epitomizes the potential of free-electron radiation. Consider an electron at velocity $\beta = v/c$ traversing a structure with periodicity a ; it generates far-field radiation at wavelength λ and polar angle θ , dictated by²

$$\lambda = \frac{a}{m} \left(\frac{1}{\beta} - \cos\theta \right) \quad (1)$$

where m is the integer diffraction order. The absence of a minimum velocity in equation (1) offers prospects for threshold-free and spectrally tunable light sources, spanning from microwave and terahertz^{14–16}, across visible^{17–19}, and towards X-ray²⁰ frequencies. In stark contrast to the simple momentum-conservation determination of wavelength and angle, there is no unified yet simple analytical equation for the radiation intensity. Previous theories offer explicit solutions only under strong assumptions (for example, assuming perfect conductors or employing effective medium descriptions) or for simple, symmetric geometries^{21–23}. Consequently, heavily numerical strategies are often an unavoidable resort^{24,25}. In general, the inherent complexity of the interactions between electrons and

photonic media have prevented a more general understanding of how pronounced spontaneous electron radiation can ultimately be for arbitrary structures, and consequently, how to design the maximum enhancement for free-electron light-emitting devices.

We begin our analysis by considering an electron (charge $-e$) of constant velocity $v\hat{x}$ traversing a generic scatterer (plasmonic or dielectric, finite or extended) of arbitrary size and material composition, as in Fig. 1a. The free current density of the electron, $\mathbf{J}(\mathbf{r}, t) = -\hat{x}ev\delta(y)\delta(z)\delta(x-vt)$, generates a frequency-dependent ($e^{-i\omega t}$ convention) incident field²⁶

$$\mathbf{E}_{\text{inc}}(\mathbf{r}, \omega) = \frac{ek_{\rho}e^{ik_{\rho}x}}{2\pi\omega\epsilon_0} [\hat{x}ik_{\rho}K_0(\kappa_{\rho}) - \hat{\rho}k_{\rho}K_1(\kappa_{\rho})] \quad (2)$$

written in cylindrical coordinates (x, ρ, ψ) ; here, K_n is the modified Bessel function of the second kind, $k_v = \omega/v$ and $k_{\rho} = \sqrt{k_v^2 - k^2} = k/\beta\gamma$ ($k = \omega/c$, free-space wavevector; $\gamma = 1/\sqrt{1-\beta^2}$, Lorentz factor). Hence, the photon emission and energy loss of free electrons can be treated as a scattering problem: the electromagnetic fields $\mathbf{F}_{\text{inc}} = (\mathbf{E}_{\text{inc}}, Z_0\mathbf{H}_{\text{inc}})^T$ (for free-space impedance Z_0) are incident on a photonic medium with material susceptibility $\overline{\chi}$ (a 6×6 tensor for a general medium), causing both absorption and far-field scattering—that is, photon emission—that together comprise electron energy loss (Fig. 1a).

As recently shown in refs 27–29, for a generic electromagnetic scattering problem, passivity—the condition that polarization currents do no net work—constrains the maximum optical response from a given incident field. Consider three power quantities derived from \mathbf{F}_{inc} and the total field \mathbf{F} within the scatterer volume V : the total power lost by the electron, $P_{\text{loss}} = -(1/2)\text{Re}\int_V \mathbf{J}^* \cdot \text{Ed}V = (\epsilon_0\omega/2)\text{Im}\int_V \mathbf{F}_{\text{inc}}^{\dagger} \overline{\chi} \mathbf{F} dV$, the power absorbed by the medium, $P_{\text{abs}} = (\epsilon_0\omega/2)\text{Im}\int_V \mathbf{F}^{\dagger} \overline{\chi} \mathbf{F} dV$, and their difference, the power radiated to the far field, $P_{\text{rad}} = P_{\text{loss}} - P_{\text{abs}}$. Treating \mathbf{F} as an independent variable, the total loss P_{loss} is a linear function of \mathbf{F} , whereas the fraction that is dissipated is a quadratic function of \mathbf{F} . Passivity requires non-negative radiated power, represented by the inequality $P_{\text{abs}} < P_{\text{loss}}$, which in this framework is therefore a convex constraint on any response function. Constrained maximization (see Supplementary Section 1) of the energy-loss and photon-emission power quantities, P_{loss} and P_{rad} , directly yields the limits

$$P_{\tau}(\omega) \leq \frac{\epsilon_0\omega\epsilon_{\tau}}{2} \int_V \mathbf{F}_{\text{inc}}^{\dagger} \overline{\chi}^{-1} (\text{Im}\overline{\chi})^{-1} \overline{\chi} \mathbf{F}_{\text{inc}} dV \quad (3)$$

¹Research Laboratory of Electronics, Massachusetts Institute of Technology, Cambridge, MA, USA. ²Institute for Soldier Nanotechnologies, Cambridge, MA, USA. ³Department of Applied Physics and Energy Sciences Institute, Yale University, New Haven, CT, USA. ⁴Andrew and Erna Viterbi Department of Electrical Engineering, Technion-Israel Institute of Technology, Haifa, Israel. *e-mail: yiy@mit.edu; owen.miller@yale.edu; kaminer@technion.ac.il

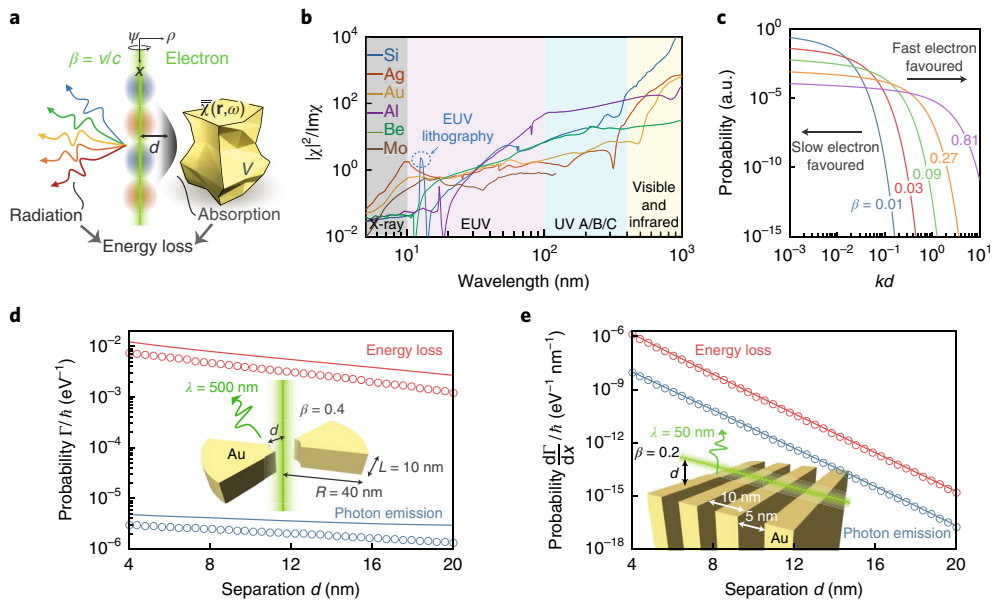


Fig. 1 | Theoretical framework and predictions. **a**, The interaction between a free electron and an obstacle defined by a susceptibility tensor (\mathbf{r}, ω) within a volume V , located at a distance d , generates electron energy loss into radiation and absorption. **b**, $|\chi|^2/\text{Im}\chi$ constrains the maximum material response to the optical excitations of free electrons over different spectral ranges for representative materials (from ref. ⁴⁰). At the X-ray and extreme ultraviolet (EUV) regime, Si is optimal near the technologically relevant 13.5 nm (dashed circle). Contrary to the image charge intuition for the optical excitations of electrons, low-loss dielectrics (such as Si in the visible and infrared regimes) can be superior to metals. **c**, Shape-independent upper limit showing superiority of slow or fast electrons at small or large separations; the material affects only the overall scaling. **d, e**, Numerical simulations (circles) compared to analytical upper limits (lines; equation (5a) for **d** and equation (6) for **e**, respectively) for the radiation (blue) and energy loss (red) of electrons penetrating the centre of an annular bowtie antenna (**d**) and passing above a grating (**e**).

where $\tau \in \{\text{rad}, \text{loss}\}$ and ξ_τ accounts for a variable radiative efficiency η (defined as the ratio of radiative to total energy loss): $\xi_{\text{loss}} = 1$ and $\xi_{\text{rad}} = \eta(1 - \eta) \leq 1/4$. Hereafter, we consider isotropic and non-magnetic materials (and thus a scalar susceptibility χ), but the generalizations to anisotropic and/or magnetic media are straightforward.

Combining equations (2) and (3) yields a general limit on the loss or emission spectral probabilities $\Gamma_\tau(\omega) = P_\tau(\omega)/\hbar\omega$:

$$\Gamma_\tau(\omega) \leq \frac{\alpha \xi_\tau c}{2\pi\omega^2} \int_V \frac{|\chi|^2}{\text{Im}\chi} [\kappa_\rho^4 K_0^2(\kappa_\rho d) + \kappa_v^2 k_v^2 K_1^2(\kappa_\rho d)] dV \quad (4)$$

where α is the fine-structure constant. Equation (4) imposes, without solving Maxwell's equations, a maximum rate of photon generation based on the electron velocity β (through k_v and κ_ρ), the material composition $\chi(\mathbf{r})$ and the volume V .

The limit in equation (4) can be further simplified by removing the shape dependence of V , since the integrand is positive and is thus bounded above by the same integral for any enclosing structure. A scatterer separated from the electron by a minimum distance d can be enclosed within a larger concentric hollow cylinder sector of inner radius d and outer radius ∞ . For such a sector (height L and opening azimuthal angle $\psi \in (0, 2\pi]$), equation (4) can be further simplified, leading to a general closed-form shape-independent limit (see Supplementary Section 2) that highlights the pivotal role of the impact parameter $\kappa_\rho d$:

$$\Gamma_\tau(\omega) \leq \frac{\alpha \xi_\tau}{2\pi c} \frac{|\chi|^2}{\text{Im}\chi} \frac{L\psi}{\beta^2} [(\kappa_\rho d) K_0(\kappa_\rho d) K_1(\kappa_\rho d)] \quad (5a)$$

$$\propto \frac{1}{\beta^2} \begin{cases} \ln(1/\kappa_\rho d) & \text{for } \kappa_\rho d \ll 1, \\ \pi e^{-2\kappa_\rho d}/2 & \text{for } \kappa_\rho d \gg 1 \end{cases} \quad (5b)$$

The limits of equations (4), (5a) and (5b) are completely general; they set the maximum photon emission and energy loss of an electron beam coupled to an arbitrary photonic environment in either the non-retarded or retarded regimes, given only the beam properties and material composition. The key factors that determine maximal radiation are identified: intrinsic material loss (represented by $\text{Im}\chi$), electron velocity β and impact parameter $\kappa_\rho d$. The metric $|\chi|^2/\text{Im}\chi$ reflects the influence of the material choice, which depends sensitively on the radiation wavelength (Fig. 1b). The electron velocity β also appears implicitly in the impact parameter $\kappa_\rho d = kd/\beta\gamma$, showing that the relevant length scale is set by the relativistic velocity of the electron. The impact parameter $\kappa_\rho d$ reflects the influence of the Lorentz contraction d/γ ; a well-known feature of both electron radiation and acceleration^{20,26,30}.

A surprising feature of the limits in equations (4), (5a) and (5b) is their prediction for optimal electron velocities. As shown in Fig. 1c, when electrons are in the far field of the structure ($\kappa_\rho d \gg 1$), stronger photon emission and energy loss are achieved by faster electrons—a well-known result. On the contrary, if electrons are in the near field ($\kappa_\rho d \ll 1$), slower electrons are optimal. This contrasting behaviour is evident in the asymptotics of equation (5b), where the $1/\beta^2$ or $e^{-2\kappa_\rho d}$ dependence is dominant at short or large separations. Physically, the optimal velocities are determined by the incident-field properties (equation (2)): slow electrons generate stronger near-field amplitudes although they are more evanescent (Supplementary Section 2). There has been recent interest in using low-energy electrons for Cherenkov¹⁰ and Smith–Purcell³¹ radiation; our prediction that they can be optimal at subwavelength interaction distances underscores the substantial technological potential of non-relativistic free-electron radiation sources.

The tightness of the limit (equations (4), (5a) and (5b)) is demonstrated by comparison with full-wave numerical calculations

(see Methods) in Fig. 1d,e. Two scenarios are considered: in Fig. 1d, an electron traverses the centre of an annular Au bowtie antenna and undergoes antenna-enabled transition radiation ($\eta \approx 0.07\%$), while, in Fig. 1e, an electron traverses a Au grating, undergoing Smith–Purcell radiation ($\eta \approx 0.9\%$). In both cases, the numerical results closely trail the upper limit at the considered wavelengths, showing that the limits can be approached or even attained with modest effort.

Next, we specialize in the canonical Smith–Purcell set-up illustrated in Fig. 1e inset. This set-up warrants a particularly close study, given its prominent historical and practical role in free-electron radiation. Aside from the shape-independent limit (equations (5a) and (5b)), we can find a sharper limit (in per unit length for periodic structure) specifically for Smith–Purcell radiation using rectangular gratings of filling factor Λ (see Supplementary Section 3)

$$\frac{d\Gamma_{\tau}(\omega)}{dx} \leq \frac{\alpha_{\zeta_{\tau}}^{\xi} |\chi|^2}{2\pi c \operatorname{Im}\chi} \Lambda \mathcal{G}(\beta, kd) \quad (6)$$

The function $\mathcal{G}(\beta, kd)$ is an azimuthal integral (see Supplementary Section 3) over the Meijer G-function $G_{1,3}^{3,0}$ (ref. 32) that arises in the radial integration of the modified Bessel functions K_n . We emphasize that equation (6) is a specific case of equation (4) for grating structures without any approximations and thus can be readily generalized to multi-material scenarios (see Supplementary equation (37)).

The grating limit (equation (6)) exhibits the same asymptotics as equations (5a) and (5b), thereby reinforcing the optimal-velocity predictions of Fig. 1c. The (β, kd) dependence of \mathcal{G} (see Fig. 2a) shows that slow (fast) electrons maximize Smith–Purcell radiation in the small (large) separation regime. We verify the limit predictions by comparison with numerical simulations: at small separations (Fig. 2b), radiation and energy loss peak at velocity $\beta \approx 0.15$, consistent with the limit maximum; at large separations (Fig. 2c), both the limit and the numerical results grow monotonically with β .

The derived upper limit also applies to Cherenkov and transition radiation, as well as bulk loss in electron energy-loss spectroscopy. For these scenarios where electrons enter material bulk, a subtlety arises for the field divergence along the electron's trajectory ($\rho = 0$ in equation (2)) within a potentially lossy medium. This divergence, however, can be regularized by introducing natural, system-specific momentum cutoffs²⁶, which then directly permits the application of our theory (see Supplementary Section 6). Meanwhile, there exist additional competing interaction processes (for example, electrons colliding with individual atoms). However, they typically occur at much smaller length scales.

We perform quantitative experimental measurement of Smith–Purcell radiation to directly probe the upper limit. Figure 3a shows our experimental set-up (see Methods and Supplementary Section 7 for details). A one-dimensional (1D) 50%-filling-factor grating (Au-covered single-crystalline Si)—the quintessential Smith–Purcell set-up—is chosen as a sample, and shown by scanning electron microscope (SEM) images in Fig. 3b,c. Free electrons pass above and impinge onto the sample at a grazing angle of 1.5° under 10 to 20 kV acceleration voltages.

Figure 3d depicts our measurements of first-order $m = 1$ Smith–Purcell radiation appearing at wavelengths between 500 and 750 nm. In quantitative agreement with equation (1) evaluated at the normal emission angle (solid lines), the measured radiation spectra (dots) blueshift with increasing electron velocity. Notably, we experimentally obtain the absolute intensity of the collected radiation via a calibration measurement (see Supplementary Section 7). The upper limits (equation (4)) for the surface-normal emission wavelengths ($\lambda = a/\beta$) are evaluated at the centre of the interaction region (height ≈ 140 nm ($kd \approx 1.5$), varying with beam energy), and is shown with shading in Fig. 3d to account for the thickness uncertainty

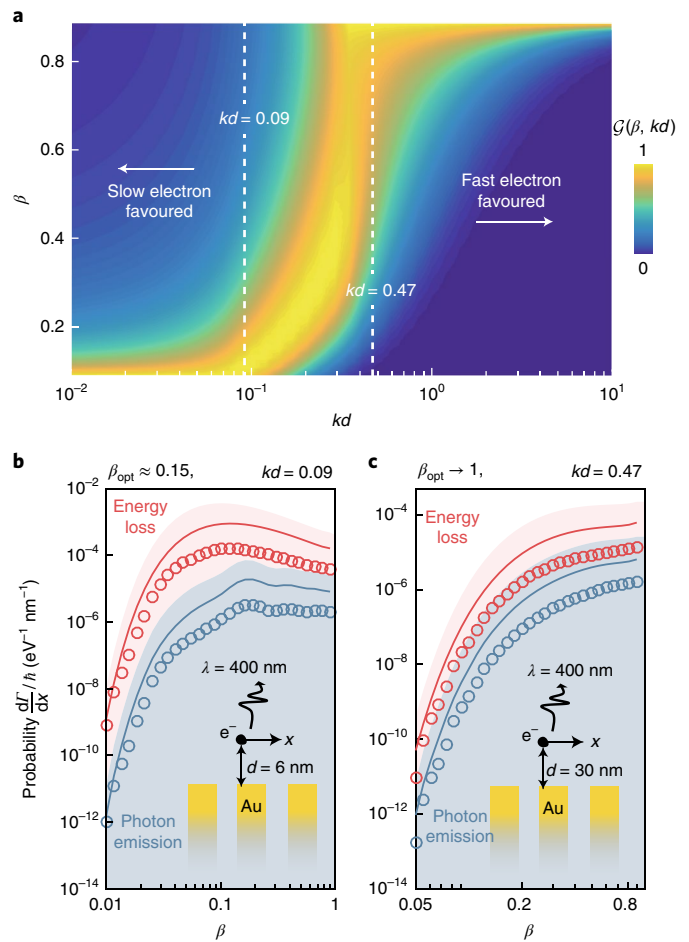


Fig. 2 | Optimal electron velocities for maximal Smith–Purcell radiation. **a**, Behaviour of $\mathcal{G}(\beta, kd)$, equation (6), whose maxima indicate separation-dependent optimal electron velocities. Here \mathcal{G} is normalized between 0 and 1 for each separation. The limit yields sharply contrasting predictions: slow electrons are optimal in the near field ($kd \ll 1$) and fast electrons are optimal in the far field ($kd \gg 1$). **b, c**, Energy loss (red) and radiation (blue) rates (circles: full-wave simulations; lines: grating limit, equation (6); shading: shape-independent limit, equations (5a) and (5b)) at two representative near/far-field separation distances (white dashed slices in **a**).

(± 1.5 nm). The envelope spanned by the measurement peaks follows the upper-limit lineshape across the visible spectrum: both the theoretical limit and the measured intensities peak near 550 nm and decrease in a commensurate manner for other wavelengths. This lineshape originates from two competing factors. At shorter wavelengths, the material factor $|\chi|^2/\operatorname{Im}\chi$ decreases significantly for both Au and Si (see Fig. 1c), which accounts for the reduced radiation intensity. At longer wavelengths, the major constraint becomes the less efficient interaction between the electrons and the structure, as the electron-beam diameters increase for the reduced brightness of the electron gun (tungsten) at lower acceleration voltages (see Supplementary Section 7). These pieces of experimental evidence for the upper limit are at $kd \approx 1.5$ (estimated from a geometrical ray-tracing model; see Supplementary Section 7), where fast electrons are still preferred (Fig. 2a). To further confirm our theory, we also conduct a near-infrared Smith–Purcell experiment (Supplementary Section 8) at $kd \approx 1$, where the envelope lineshape of the emission spectra again follows our prediction. We also obtain complementary supporting evidence (extracted from a recent work¹⁰) for our slow-electron-efficient prediction (see Supplementary Section 9).

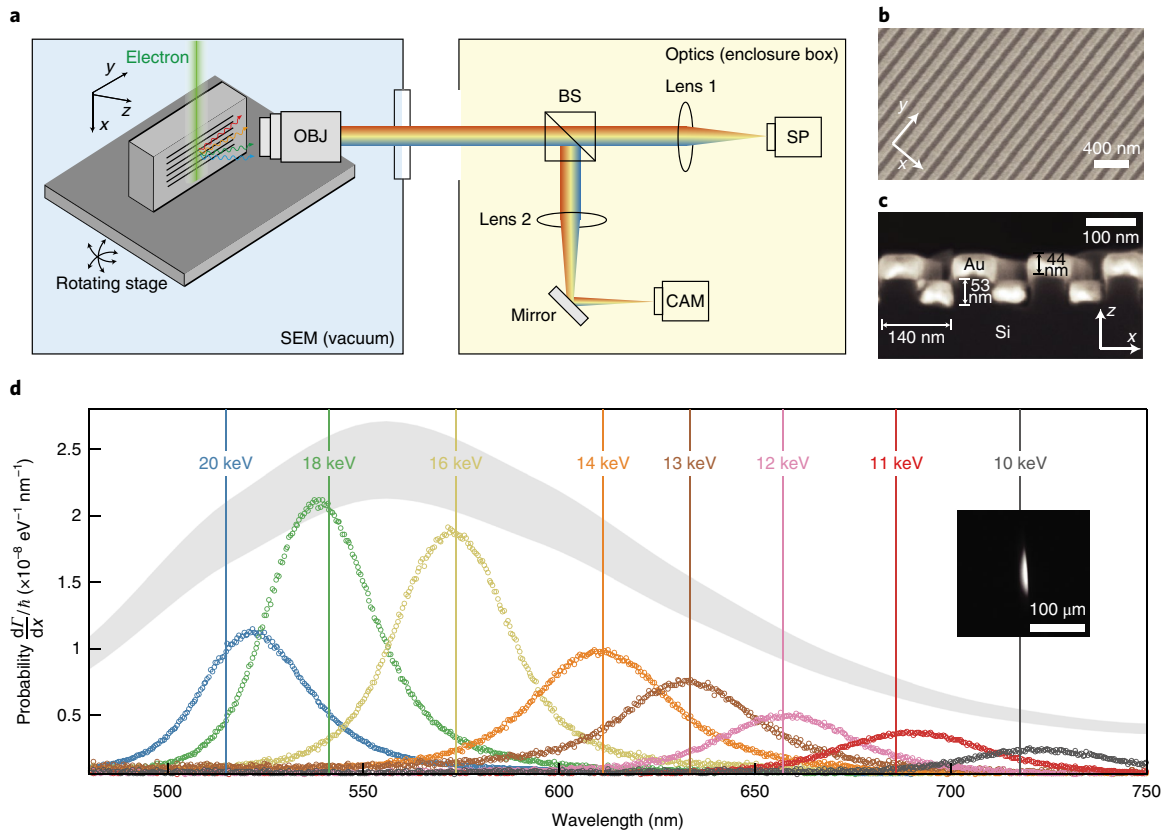


Fig. 3 | Experimental probing of the upper limit. **a**, Experimental set-up. OBJ, objective (numerical aperture of 0.3); BS, beamsplitter; SP, spectrometer; CAM, camera. **b,c**, SEM images of the structure in top view (**b**) and cross-sectional view (**c**). **d**, Quantitative measurement of Smith–Purcell radiation (inset: camera image of the radiation). The solid lines mark the theoretical radiation wavelengths at the normal angle (equation (1)). The envelope (peak outline) of the measured spectra (dots) follows the theoretical upper limit (shaded to account for fabrication tolerance; calculated at each wavelength with the corresponding electron velocity for surface-normal radiation).

Finally, we turn our attention to an ostensible peculiarity of the limits: equation (4) evidently diverges for lossless materials ($\text{Im}\chi \rightarrow 0$), seemingly providing little insight. On the contrary, this divergence suggests the existence of a mechanism capable of strongly enhancing Smith–Purcell radiation. Indeed, by exploiting high- Q resonances near bound states in the continuum (BICs)¹³ in photonic crystal slabs, we find that Smith–Purcell radiation can be enhanced by orders of magnitude, when specific frequency-, phase- and polarization-matching conditions are met.

A 1D silicon ($\chi = 11.25$)-on-insulator (SiO_2 , $\chi = 1.07$) grating interacting with a sheet electron beam illustrates the core conceptual idea most clearly. The transverse electric (TE) (E_x, H_y, E_z) band structure (lowest two bands labelled TE_0 and TE_1), matched polarization for a sheet electron beam (supplementary equation S41b), is depicted in Fig. 4b along the Γ – X direction. Folded electron wavevectors, $k_v = \omega/v$, are overlaid for two distinct velocities (blue and green). Strong electron–photon interactions are possible when the electron and photon dispersions intersect: for instance, k_v and the TE_0 band intersect (grey circles) below the air light cone (light yellow shading). However, these intersections are largely impractical: the TE_0 band is evanescent in the air region, precluding free-space radiation. Still, analogous ideas, employing similar partially guided modes, such as spoof plasmons³³, have been explored for generating electron-enabled guided waves^{34,35}.

To overcome this deficiency, we theoretically propose a new mechanism for enhanced Smith–Purcell radiation: coupling of electrons with BICs¹³. The latter have the extreme quality factors of guided modes but are, crucially, embedded in the radiation continuum, guaranteeing any resulting Smith–Purcell radiation into

the far field. By choosing appropriate velocities $\beta = a/m\lambda$ (m being any integer; λ being the BIC wavelength) such that the electron line (blue or green) intersects the TE_1 mode at the BIC (red square in Fig. 4b), the strong enhancements of a guided mode can be achieved in tandem with the radiative coupling of a continuum resonance. In Fig. 4c, the incident fields of electrons and the field profile of the BIC indicate their large modal overlaps. The BIC field profile shows complete confinement without radiation, unlike conventional multipolar radiation modes (see Supplementary Fig. 9). The Q values of the resonances are also provided near a symmetry-protected BIC¹³ at the Γ point. Figure 4d,e demonstrates the velocity tunability of BIC-enhanced radiation—as the phase matching approaches the BIC, a divergent radiation rate is achieved.

The BIC-enhancement mechanism is entirely accordant with our upper limits. Practically, silicon has non-zero loss across the visible and near-infrared wavelengths. For example, for a period of $a = 676$ nm, the optimally enhanced radiation wavelength is $\approx 1,050$ nm, at which $\chi_{\text{Si}} \approx 11.25 + 0.001i$ (ref. 36). For an electron–structure separation of 300 nm, we theoretically show in Fig. 4f the strong radiation enhancements (>3 orders of magnitude) attainable by BIC-enhanced coupling. The upper limit (shaded region; 2D analogue of equation (4); see Supplementary Section 10) attains extremely large values due to the minute material loss ($|\chi|^2 / \text{Im}\chi \approx 10^5$); nevertheless, BIC-enhanced coupling enables the radiation intensity to closely approach this limit at several resonant velocities. In the presence of an absorptive channel, the maximum enhancement occurs at a small offset from the BIC where the Q -matching condition (see Supplementary Section 11) is satisfied (that is, equal absorptive and radiative rates of the resonances).

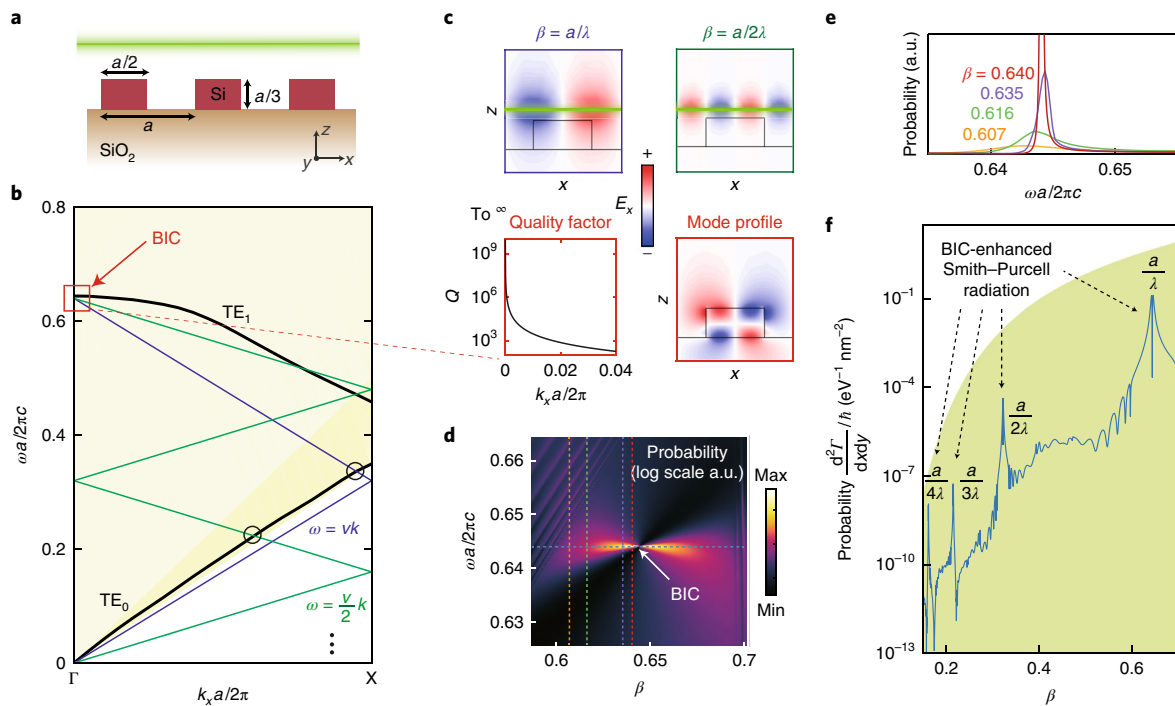


Fig. 4 | Strong enhancement of Smith–Purcell radiation via high-Q resonances near a photonic BIC. **a**, A schematic drawing of a silicon-on-insulator grating (1D photonic crystal slab: periodic in x and infinite in y). **b**, The calculated TE band structure (solid black lines) in the Γ – X direction. The area shaded in light and dark yellow indicates the light cone of air and silica, respectively. The electron lines (blue for velocity v , and green for $v/2$) can phase match with either the guided modes (circles) or high-Q resonances near a BIC (red square). **c**, Upper: incident field of electrons. Lower: resonant quality factors (left) and eigenmode profile (right) near a BIC. **d**, Strongly enhanced Smith–Purcell radiation near the BIC. **e**, Vertical slices of **d**. **f**, The limit (shaded area) compared with the horizontal slice of **d**, with material loss considered. Strong enhancement happens at electron velocities $\beta = a/m\lambda$ ($m = 1, 2, 3 \dots$).

In closing, we have theoretically derived and experimentally probed a universal upper limit to the energy loss and photon emission from free electrons. The limit depends crucially on the impact parameter $\kappa_\rho d$, but not on any other detail of the geometry. Hence, our limit applies even to the most complex metamaterials and metasurfaces, given only their constituents. Surprisingly, in the near field, slow electrons promise stronger radiation than relativistic ones. The limit predicts a divergent radiation rate as the material loss rate goes to zero, and we show that BIC resonances enable such staggering enhancements. This is relevant for the generation of coherent Smith–Purcell radiation^{14,34,35}. The long lifetime, spectral selectivity and large field enhancement near a BIC can strongly bunch electrons, allowing them to radiate coherently at the same desired frequency, potentially enabling low-threshold Smith–Purcell free-electron lasers. The combination of this mechanism and the optimal velocity prediction reveals prospects of low-voltage yet high-power free-electron radiation sources. In addition, our findings demonstrate a simple guiding principle to maximize the signal-to-noise ratio for electron energy-loss spectroscopy through an optimal choice of electron velocity, enabling improved spectral resolution.

The predicted slow-electron-efficient regime still calls for direct experimental validation. We suggest that field-emitter-integrated free-electron devices (for example, ref.¹⁰) are ideal to confirm the prediction due to the achievable small electron–structure separation and high electron beam quality at relatively large currents. Alternatively, the microwave or terahertz frequencies could be suitable spectral ranges for verifying the slow-electron-efficient regime, where the subwavelength separation requirement is more achievable.

The upper limit demonstrated here is in the spontaneous emission regime for constant-velocity electrons, and can be extended to the stimulated regime by suitable reformulation. Stronger electron–photon interactions can change electron velocity by a non-negligible amount that alters the radiation. If necessary, this correction can be perturbatively incorporated. In the case of external optical pumping³⁷, the upper limit can be revised by redefining the incident field as the summation of the electron incident field and the external optical field. From a quantum mechanical perspective, this treatment corresponds to stimulated emission from free electrons, which multiplies the limit by the number of photons in that radiation mode. This treatment could also potentially translate our limit into a fundamental limit for particle acceleration^{38,39}, which is the time-reversal of free-electron energy loss and which typically incorporates intense laser pumping. In the multi-electron scenario, the radiation upper limit will be obtained in the case of perfect bunching, where all electrons radiate in phase. In this case, our single-electron limit should be multiplied by the number of electrons to correct for the superradiant nature of such coherent radiation.

Methods

Methods, including statements of data availability and any associated accession codes and references, are available at <https://doi.org/10.1038/s41567-018-0180-2>

Received: 18 December 2017; Accepted: 17 May 2018;

Published online: 16 July 2018

References

- Cherenkov, P. A. Visible glow under exposure of gamma radiation. *Dokl. Akad. Nauk SSSR* **2**, 451–454 (1934).

2. Smith, S. J. & Purcell, E. Visible light from localized surface charges moving across a grating. *Phys. Rev.* **92**, 1069 (1953).
3. Ginsburg, V. & Frank, I. Radiation of a uniformly moving electron due to its transition from one medium into another. *Zh. Eksp. Teor. Fiz.* **16**, 15–28 (1946).
4. Goldsmith, P. & Jelley, J. Optical transition radiation from protons entering metal surfaces. *Philos. Mag.* **4**, 836–844 (1959).
5. Liu, S. et al. Surface polariton Cherenkov light radiation source. *Phys. Rev. Lett.* **109**, 153902 (2012).
6. Kaminer, I. et al. Efficient plasmonic emission by the quantum Čerenkov effect from hot carriers in graphene. *Nat. Commun.* **7**, ncomms11880 (2016).
7. Luo, C., Ibanescu, M., Johnson, S. G. & Joannopoulos, J. Čerenkov radiation in photonic crystals. *Science* **299**, 368–371 (2003).
8. Adamo, G. et al. Light well: a tunable free-electron light source on a chip. *Phys. Rev. Lett.* **103**, 113901 (2009).
9. Ginis, V., Danckaert, J., Veretennicoff, I. & Tassin, P. Controlling Čerenkov radiation with transformation-optical metamaterials. *Phys. Rev. Lett.* **113**, 167402 (2014).
10. Liu, F. et al. Integrated Čerenkov radiation emitter eliminating the electron velocity threshold. *Nat. Photon.* **11**, 289–292 (2017).
11. Hsu, C. W. et al. Observation of trapped light within the radiation continuum. *Nature* **499**, 188–191, (2013).
12. Yang, Y., Peng, C., Liang, Y., Li, Z. & Noda, S. Analytical perspective for bound states in the continuum in photonic crystal slabs. *Phys. Rev. Lett.* **113**, 037401 (2014).
13. Hsu, C. W., Zhen, B., Stone, A. D., Joannopoulos, J. D. & Soljacic, M. Bound states in the continuum. *Nat. Rev. Mater.* **1**, 16048 (2016).
14. Urata, J. et al. Superradiant Smith–Purcell emission. *Phys. Rev. Lett.* **80**, 516–519 (1998).
15. Korbly, S., Kesar, A., Sirigiri, J. & Temkin, R. Observation of frequency-locked coherent terahertz Smith–Purcell radiation. *Phys. Rev. Lett.* **94**, 054803 (2005).
16. Doucas, G., Mulvey, J., Omori, M., Walsh, J. & Kimmitt, M. First observation of Smith–Purcell radiation from relativistic electrons. *Phys. Rev. Lett.* **69**, 1761–1764 (1992).
17. Kube, G. et al. Observation of optical Smith–Purcell radiation at an electron beam energy of 855 MeV. *Phys. Rev. E* **65**, 056501 (2002).
18. Yamamoto, N., de Abajo, F. J. G. & Myroshnychenko, V. Interference of surface plasmons and Smith–Purcell emission probed by angle-resolved cathodoluminescence spectroscopy. *Phys. Rev. B* **91**, 125144 (2015).
19. Kaminer, I. et al. Spectrally and spatially resolved Smith–Purcell radiation in plasmonic crystals with short-range disorder. *Phys. Rev. X* **7**, 011003 (2017).
20. Moran, M. J. X-ray generation by the Smith–Purcell effect. *Phys. Rev. Lett.* **69**, 2523–2526 (1992).
21. van den Berg, P. Smith–Purcell radiation from a point charge moving parallel to a reflection grating. *J. Opt. Soc. Am.* **63**, 1588–1597 (1973).
22. Haeblerlé, O., Rullhusen, P., Salomé, J.-M. & Maene, N. Calculations of Smith–Purcell radiation generated by electrons of 1–100 MeV. *Phys. Rev. E* **49**, 3340–3352 (1994).
23. Sergeeva, D. Y., Tishchenko, A. & Strikhanov, M. Conical diffraction effect in optical and x-ray Smith–Purcell radiation. *Phys. Rev. ST Accel. Beams* **18**, 052801 (2015).
24. Pendry, J. & Martin-Moreno, L. Energy loss by charged particles in complex media. *Phys. Rev. B* **50**, 5062–5073 (1994).
25. García de Abajo, F. J. Smith–Purcell radiation emission in aligned nanoparticles. *Phys. Rev. E* **61**, 5743–5752 (2000).
26. García de Abajo, F. J. Optical excitations in electron microscopy. *Rev. Mod. Phys.* **82**, 209–275 (2010).
27. Miller, O. D. et al. Fundamental limits to optical response in absorptive systems. *Opt. Express* **24**, 3329–3364 (2016).
28. Yang, Y., Miller, O. D., Christensen, T., Joannopoulos, J. D. & Soljačić, M. Low-loss plasmonic dielectric nanoresonators. *Nano Lett.* **17**, 3238–3245 (2017).
29. Miller, O. D., Johnson, S. G. & Rodriguez, A. W. Shape-independent limits to near-field radiative heat transfer. *Phys. Rev. Lett.* **115**, 204302 (2015).
30. Friedman, A., Gover, A., Kurizki, G., Ruschin, S. & Yariv, A. Spontaneous and stimulated emission from quasifree electrons. *Rev. Mod. Phys.* **60**, 471–535 (1988).
31. Massuda, A. et al. Preprint at <https://arxiv.org/abs/1710.05358> (2017).
32. Gradshteyn, I. S. & Ryzhik, I. M. in *Tables of Integrals, Series, and Products* 6th edn (eds Jeffrey, A. & Zwillinger, D.) 843–850 and 1022–1025 (Academic, San Diego, CA, 2000).
33. Pendry, J., Martin-Moreno, L. & Garcia-Vidal, F. Mimicking surface plasmons with structured surfaces. *Science* **305**, 847–848 (2004).
34. Andrews, H. L. & Brau, C. A. Gain of a Smith–Purcell free-electron laser. *Phys. Rev. ST Accel. Beams* **7**, 070701 (2004).
35. Kumar, V. & Kim, K.-J. Analysis of Smith–Purcell free-electron lasers. *Phys. Rev. E* **73**, 026501 (2006).
36. Green, M. A. Self-consistent optical parameters of intrinsic silicon at 300 K including temperature coefficients. *Sol. Energy Mater. Sol. Cells* **92**, 1305–1310 (2008).
37. Schächter, L. & Ron, A. Smith–Purcell free-electron laser. *Phys. Rev. A* **40**, 876–896 (1989).
38. Peralta, E. A. et al. Demonstration of electron acceleration in a laser-driven dielectric microstructure. *Nature* **503**, 91–94 (2013).
39. Breuer, J. & Hommelhoff, P. Laser-based acceleration of nonrelativistic electrons at a dielectric structure. *Phys. Rev. Lett.* **111**, 134803 (2013).
40. Palik, E. D. *Handbook of Optical Constants of Solids* Vol. 3 (Academic, San Diego, CA, 1998).

Acknowledgements

The authors acknowledge fruitful discussions with K. Berggren, S. Yang, C. Peng, A. Gover, B. Zhen, L. J. Wong, X. Lin, D. Zhu, Yu. Yang, T. Dubcek and N. Rivera. We thank P. Rebusco for critical reading and editing of the manuscript. This work was performed in part at the Harvard University Center for Nanoscale Systems (CNS), a member of the National Nanotechnology Coordinated Infrastructure Network (NNCI), which is supported by the National Science Foundation under NSF ECCS award no. 1541959. This work was partly supported by the Army Research Office through the Institute for Soldier Nanotechnologies under contract nos W911NF-18-2-0048 and W911NF-13-D-0001. Y.Y. was partly supported by the MRSEC Program of the National Science Foundation under grant no. DMR-1419807. T.C. was supported by the Danish Council for Independent Research (grant no. DFFC6108-00667). O.D.M. was supported by the Air Force Office of Scientific Research under award no. FA9550-17-1-0093. I.K. was partially supported by the Azrieli foundation and the Seventh Framework Programme of the European Research Council (FP7- Marie Curie IOF) under grant agreement no. 328853CMC-BSiCS.

Author contributions

Y.Y., O.D.M., I.K. and M.S. conceived the project. Y.Y. developed the analytical models and numerical calculations. A.M. prepared the sample under study. Y.Y., A.M., C.R.-C., S.E.K. and I.K. performed the experiment. Y.Y., T.C. and O.D.M. analysed the asymptotics and bulk loss of the limit. S.G.J., J.D.J., O.D.M., I.K. and M.S. supervised the project. Y.Y. wrote the manuscript with input from all authors.

Competing interests

The authors declare no competing interests.

Additional information

Supplementary information is available for this paper at <https://doi.org/10.1038/s41567-018-0180-2>.

Reprints and permissions information is available at www.nature.com/reprints.

Correspondence and requests for materials should be addressed to Y.Y. or O.D.M. or I.K.

Publisher's note: Springer Nature remains neutral with regard to jurisdictional claims in published maps and institutional affiliations.

Methods

Fourier transform convention. Throughout the paper, we adopt the following Fourier transform conventions

$$f(\omega) \triangleq \int f(t) e^{i\omega t} dt, \quad f(t) \triangleq \frac{1}{2\pi} \int f(\omega) e^{-i\omega t} d\omega \quad (7)$$

$$g(\mathbf{k}) \triangleq \int f(\mathbf{r}) e^{-i\mathbf{k}\cdot\mathbf{r}} d\mathbf{r}, \quad g(\mathbf{r}) \triangleq \frac{1}{(2\pi)^3} \int g(\mathbf{k}) e^{i\mathbf{k}\cdot\mathbf{r}} d\mathbf{k} \quad (8)$$

Numerical methods. The photonic band structure in Fig. 4b is calculated via the eigenfrequency calculation in COMSOL Multiphysics. Numerical radiation intensities (Figs. 1d,e, 2b,c, 3d and 4d–f) are obtained via the frequency-domain calculation in the radiofrequency module in COMSOL Multiphysics. A surface (for 3D problems) or line (for 2D problems) integral on the Poynting vector is calculated to extract the radiation intensity at each frequency.

Experimental set-up and sample fabrication. Our experimental set-up comprises a conventional SEM with the sample mounted perpendicular to the stage. A microscope objective was placed on the SEM stage to collect and image the light emission from the surface. The collected light was then sent through a series of

free-space optical elements, enabling simultaneous measurement of the spectrum and of the spatial radiation pattern.





The SEM used for the experiment was a JEOL JSM-6010LA. Its energy spread at the gun exit was in the range 1.5 to 2.5 eV for the range of acceleration voltages considered in this paper. The SEM was operated in spot mode, which we controlled precisely to align the beam so that it passes tangentially to the surface near the desired area of the sample. A Nikon TU Plan Fluor 10x objective with a numerical aperture of 0.30 was used to collect light from the area of interest. The monochrome image of the radiation was taken using a Hamamatsu CCD (charge-coupled device). The spectrometer used was an Action SP-2360-2300i with a low-noise Princeton Instruments Pixis 400 CCD.

A 1D grating (Au-covered single-crystalline Si: periodicity, 140 nm; filling factor, 50%; patterned Si thickness, 53 ± 1.5 nm; Au thickness 44 ± 1.5 nm) was used as the sample in our experiment. The original nanopatterned linear silicon stamp was obtained from LightSmyth Technologies and coated using an electron beam evaporator with a 2 nm Ti adhesion layer and 40 nm of Au at 10^{-7} torr. The sample was mounted inside the SEM chamber to enable the alignment of free electrons to pass in close proximity to the stamps. The emitted light was coupled out of the SEM chamber to a spectrometer, while a camera was used to image the surface of the sample.

Data availability. The data that support the plots within this paper and other findings of this study are available from the corresponding author upon reasonable request.

In the format provided by the authors and unedited.

Maximal spontaneous photon emission and energy loss from free electrons

Yi Yang ^{1*}, Aviram Massuda¹, Charles Roques-Carmes ¹, Steven E. Kooi ², Thomas Christensen¹, Steven G. Johnson¹, John D. Joannopoulos^{1,2}, Owen D. Miller ^{3*}, Ido Kaminer ^{1,4*} and Marin Soljačić¹

¹Research Laboratory of Electronics, Massachusetts Institute of Technology, Cambridge, MA, USA. ²Institute for Soldier Nanotechnologies, Cambridge, MA, USA. ³Department of Applied Physics and Energy Sciences Institute, Yale University, New Haven, CT, USA. ⁴Andrew and Erna Viterbi Department of Electrical Engineering, Technion-Israel Institute of Technology, Haifa, Israel. *e-mail: yiy@mit.edu; owen.miller@yale.edu; kaminer@technion.ac.il

13 I. GENERAL OPTICAL RESPONSE LIMIT FRAMEWORK

14 Intuitively, to impose the general limits on the energy loss and photon emission (cathodolumi-
 15 nescence) from free electrons, we consider an arbitrary scatterer embedded in a possibly hetero-
 16 geneous background. Passivity, which implies the absence of gain and that polarization currents
 17 do no work [1] requires that the absorbed (P_{abs}) and scattered (P_{rad}) powers by the target body are
 18 non-negative. On the other hand, their sum, the electron energy loss ($P_{\text{loss}} = P_{\text{abs}} + P_{\text{rad}}$), is given
 19 by the real part of the overlap between the electron velocity and the induced field [2], similar to
 20 the optical theorem [3].

21 More broadly, for an arbitrarily shaped 3D scatterer [volume V and susceptibility tensor $\chi(r, \omega)$]
 22 impinged by the external incident field $\mathbf{F}_{\text{inc}} = (\mathbf{E}_{\text{inc}}, Z_0 \mathbf{H}_{\text{inc}})^T$ [for the case of free electrons, see
 23 Eq. (2)], the absorption (dissipation) within such a medium is the work done by the total fields \mathbf{F}
 24 on the induced currents, given by the expression

$$25 \quad P_{\text{abs}} = \frac{\epsilon_0 \omega}{2} \text{Im} \int_V \mathbf{F}^\dagger \chi \mathbf{F} dV. \quad (S1)$$

27 On the other hand, the total electron energy loss represents the work done by the incident fields on
 28 the induced currents

$$29 \quad P_{\text{loss}} = \frac{\epsilon_0 \omega}{2} \text{Im} \int_V \mathbf{F}_{\text{inc}}^\dagger \chi \mathbf{F} dV. \quad (S2)$$

31 As can be seen, Electron total energy loss and absorption are linear and quadratic function
 32 of the fields, respectively. Yet electron energy loss must be greater than absorption (due to the
 33 nonnegative scattering noted above), requiring the linear functional to be greater than the quadratic
 34 one, a condition that cannot be satisfied for large enough currents. The inequality $P_{\text{abs}} \leq P_{\text{loss}}$
 35 thereby provides a convex constraint for the optical excitation of free electrons. Thanks to the
 36 convex nature of the constraint $P_{\text{abs}} \leq P_{\text{loss}}$ and the simple expressions of the absorption and
 37 energy loss, the optimal response can be solved analytically using variational derivatives, without
 38 the requirement of solving the highly nonconvex Maxwell equations, thereby providing general
 39 upper-limit expressions for electron energy loss and photon emission without approximation.

40 To obtain the extremum induced fields/currents for electron energy loss or photon emission
 41 (cathodoluminescence), one can take the derivative $\frac{\partial P_\tau(\omega)}{\partial \mathbf{F}^\dagger} = 0$, where $\tau \in \{\text{rad}, \text{loss}\}$. Using the
 42 photon emission as an example, by taking

$$43 \quad \frac{\partial P_{\text{rad}}(\omega)}{\partial \mathbf{F}^\dagger} = \frac{\partial (P_{\text{loss}} - P_{\text{abs}})}{\partial \mathbf{F}^\dagger} = 0, \quad (S3)$$

45 we have

$$46 \quad \chi^\dagger \mathbf{F}_{\text{inc}}/2i + (\text{Im}\chi)\mathbf{F} = 0, \quad (S4)$$

48 where $\text{Im}\chi = (\chi - \chi^\dagger)/2i$ is a Hermitian matrix. From Eq. (S4), one readily finds the optimal total
 49 field is given by $\mathbf{F}_{\text{rad,opt}} = \frac{i}{2}(\text{Im}\chi)^{-1}\chi^\dagger \mathbf{F}_{\text{inc}}$. The optimal field for maximal electron energy loss
 50 can be derived in a similar manner. Combining the optimal fields with Eq. (S1) and Eq. (S2), we
 51 obtain the upper limit shown in Eq. (3) in the main text.

52 II. THREE-DIMENSIONAL SHAPE-INDEPENDENT UPPER LIMIT

53 We first rewrite the three-dimensional general limit equation

$$54 \quad \Gamma_\tau(\omega) \leq \frac{e^2 \xi_\tau}{8\hbar\epsilon_0\omega^2\pi^2} \int_V \frac{|\chi|^2}{\text{Im}\chi} \left[\kappa_\rho^4 K_0^2(\kappa_\rho\rho) + \kappa_\rho^2 k_v^2 K_1^2(\kappa_\rho\rho) \right] dV. \quad (S5)$$

55 We assume the structure is made of a single material

$$56 \quad \Gamma_\tau(\omega) \leq \frac{e^2 \xi_\tau}{8\hbar\epsilon_0\omega^2\pi^2} \frac{|\chi|^2}{\text{Im}\chi} \int_V \left[\kappa_\rho^4 K_0^2(\kappa_\rho\rho) + \kappa_\rho^2 k_v^2 K_1^2(\kappa_\rho\rho) \right] dV. \quad (S6)$$

57 We now simplify the integral

$$58 \quad \mathcal{K} = \int_V \left[\kappa_\rho^4 K_0^2(\kappa_\rho\rho) + \kappa_\rho^2 k_v^2 K_1^2(\kappa_\rho\rho) \right] dV. \quad (S7)$$

59 For an arbitrarily-shaped structure, whether isolated or extended, one can always find a circular
 60 concentric hollow cylinder (height L , opening azimuthal angle $\psi \in [0, 2\pi]$, minor radius being the
 61 electron structure separation, major radius can be finite or infinite) that encloses it. Therefore, we
 62 can evaluate the integral in the cylindrical coordinate

$$\begin{aligned} 63 \quad \mathcal{K} &\leq L\psi \int_d^\infty \rho \left[\kappa_\rho^4 K_0^2(\kappa_\rho\rho) + \kappa_\rho^2 k_v^2 K_1^2(\kappa_\rho\rho) \right] d\rho \\ 64 \quad &= L\psi \int_{x_0}^\infty x \left[\kappa_\rho^2 K_0^2(x) + k_v^2 K_1^2(x) \right] dx, \\ 65 \quad &= \frac{x_0^2}{2} \left\{ \kappa_\rho^2 \left[K_1^2(x_0) - K_0^2(x_0) \right] + k_v^2 \left[K_0(x_0)K_2(x_0) - K_1^2(x_0) \right] \right\}, \\ 66 \quad &= \frac{x_0^2}{2} \left\{ k_v^2 K_0(x_0) \left[K_2(x_0) - K_0(x_0) \right] - k^2 \left[K_1^2(x_0) - K_0^2(x_0) \right] \right\}, \\ 67 \quad &= x_0 k_v^2 K_0(x_0) K_1(x_0) - x_0^2 k^2 \left[K_1^2(x_0) - K_0^2(x_0) \right], \\ 68 \quad &\leq x_0 k_v^2 K_0(x_0) K_1(x_0), \quad (S8) \\ 69 \end{aligned}$$

70 where $x_0 = \kappa_\rho d$. Eq. (S8) corresponds to Eq. (5a) in the maintext. In the derivation above, we use
 71 the following relations [4]

$$72 \quad \int x K_n^2(x) dx = \frac{x^2}{2} [K_n^2(x) - K_{n-1}(x)K_{n+1}(x)], \quad (\text{S9a})$$

$$73 \quad K_{-1}(x) = K_1(x), \quad (\text{S9b})$$

$$74 \quad K_2(x) - K_0(x) = 2K_1(x)/x, \quad (\text{S9c})$$

$$75 \quad K_1(x) > K_0(x). \quad (\text{S9d})$$

77

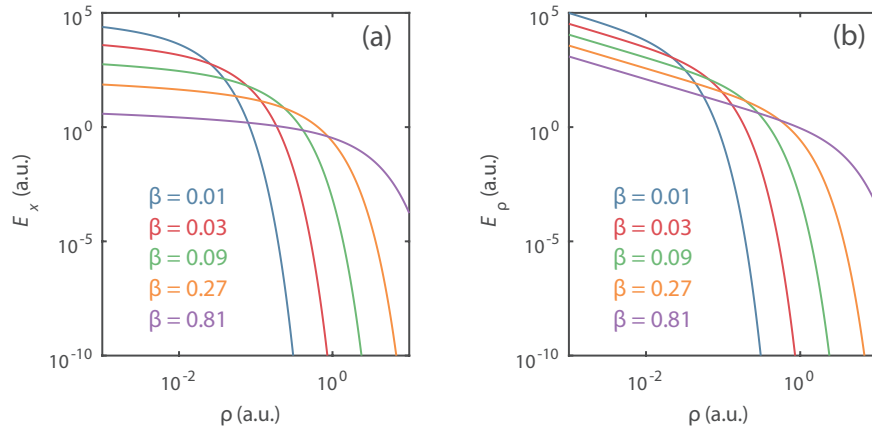


Figure S1. (a) Longitudinal E_x and (b) transverse E_ρ incident field amplitudes generated from free electrons
 78 in the azimuthal direction ρ at different velocities β .

79

80 In the main text, the shape-independent limit has sharply-contrasting prediction on the intensity
 81 of luminescence and energy loss of free electrons when they are in either the far or near field
 82 [Eq. (5b)]. Fig. S1 shows that the incident fields already exhibit similar property, which naturally
 83 translates into the upper limit via the overlap integral [Eq. (4)].

84 III. SMITH-PURCELL RADIATION UPPER LIMIT IN THREE DIMENSIONS FOR RECTAN- 85 GULAR GRATINGS

86 We choose coordinates such that (vt, y_0, z_0) depicts the trajectory of the charged particle. In the
 87 cylindrical coordinate (ρ, ψ, x) , the current density can be rewritten as

$$88 \quad \mathbf{J}(\mathbf{r}, t) = \frac{-ev}{2\pi\rho} \delta(x - vt) \delta(\rho) \hat{\mathbf{x}}. \quad (\text{S10})$$

89 Fourier transform on Eq. (S10) yields the current density in the frequency domain

$$90 \quad \mathbf{J}(\mathbf{r}, \omega) = \frac{-e}{2\pi\rho} e^{ik_v x} \delta(\rho) \hat{\mathbf{x}}, \quad (\text{S11})$$

91 whose external electromagnetic field is given by [5]

$$\begin{aligned} 92 \quad \mathbf{E}_{\text{inc}}(\mathbf{r}, \omega) &= \frac{e}{4\omega\epsilon_0} (k^2 \hat{\mathbf{x}} + ik_v \nabla) H_0^{(1)}(i\kappa_\rho \rho) e^{ik_v x}, \\ &= \frac{e}{4\omega\epsilon_0} [(k^2 - k_v^2) H_0^{(1)}(i\kappa_\rho \rho) \hat{\mathbf{x}} + ik_v d_\rho H_0^{(1)}(i\kappa_\rho \rho) \hat{\rho}] e^{ik_v x}, \\ 93 \quad &= \frac{e}{2\pi\omega\epsilon_0} [i\kappa_\rho^2 K_0(\kappa_\rho \rho) \hat{\mathbf{x}} - \kappa_\rho k_v K_1(\kappa_\rho \rho) \hat{\rho}] e^{ik_v x}. \end{aligned} \quad (\text{S12})$$

94 where $H_0^{(1)}$ is the Hankel function of the first kind with zero order. Here we utilize the relation
95 $K_0(z) = \frac{i\pi}{2} H_0^{(1)}(iz)$, where z is a real argument. Insert Eq. (S12) into Eq. (3) yields the general
96 three-dimensional limit shown in Eq. (4).

97 Next we consider Smith–Purcell radiation from rectangular gratings in three dimensions. The
98 volume integral of the evanescent field is given by

$$99 \quad \int_V |\mathbf{E}(\mathbf{r})|^2 dV = \frac{e^2}{4\omega^2 \epsilon_0^2 \pi^2} \int dx \int_{-\pi/2}^{\pi/2} d\psi \int_{d/\cos\psi}^{\infty} \rho d\rho [\kappa_\rho^4 K_0^2(\kappa_\rho \rho) + \kappa_\rho^2 k_v^2 K_1^2(\kappa_\rho \rho)]. \quad (\text{S13})$$

100 Closed-form integral can be obtained by using the relation

$$101 \quad \int_{d/\cos\psi}^{\infty} \rho d\rho K_0^2(\kappa_\rho \rho) = \frac{\sqrt{\pi}}{4\kappa_\rho^2} G_{1,3}^{3,0}(\kappa_\rho^2 d^2 \sec^2 \psi |_{0,1,1}), \quad (\text{S14})$$

102 and

$$103 \quad \int_{d/\cos\psi}^{\infty} \rho d\rho K_1^2(\kappa_\rho \rho) = \frac{\sqrt{\pi}}{4\kappa_\rho^2} G_{1,3}^{3,0}(\kappa_\rho^2 d^2 \sec^2 \psi |_{0,0,2}). \quad (\text{S15})$$

104 Here G is the Meijer G-function [4, 6] defined as a line integral in the complex plane

$$105 \quad G_{p,q}^{m,n} \left(z \mid \begin{matrix} a_1, \dots, a_p \\ b_1, \dots, b_q \end{matrix} \right) = \frac{1}{2\pi i} \int_L \frac{\prod_{j=1}^m \Gamma(b_j - s) \prod_{j=1}^n \Gamma(1 - a_j + s)}{\prod_{j=m+1}^q \Gamma(1 - b_j + s) \prod_{j=n+1}^p \Gamma(a_j - s)} z^s ds, \quad (\text{S16})$$

106 where Γ is the gamma function.

107 Plug Eq. (S14) and Eq. (S15) into Eq. (4) yields Eq. (6) in the main text

$$108 \quad \frac{d\Gamma_\tau(\omega)}{dx} \leq \frac{\alpha \xi_\tau}{2\pi c} \frac{|\chi|^2}{\text{Im}\chi} \Lambda \mathcal{G}(\beta, kd), \quad (\text{S17a})$$

109 where

$$110 \quad \mathcal{G}(\beta, kd) = \mathcal{G}_x(\beta, kd) + \mathcal{G}_\rho(\beta, kd), \quad (\text{S17b})$$

$$111 \quad \mathcal{G}_x(\beta, kd) = \frac{\sqrt{\pi}}{4} \int_{-\pi/2}^{\pi/2} \frac{d\psi}{\beta^2 \gamma^2} G_{3,0}^{1,3} \left(\frac{k^2 d^2}{\beta^2 \gamma^2} \sec^2 \psi \mid_{0,1,1} \right), \quad (\text{S17c})$$

$$112 \quad \mathcal{G}_\rho(\beta, kd) = \frac{\sqrt{\pi}}{4} \int_{-\pi/2}^{\pi/2} \frac{d\psi}{\beta^2} G_{3,0}^{1,3} \left(\frac{k^2 d^2}{\beta^2 \gamma^2} \sec^2 \psi \mid_{0,0,2} \right). \quad (\text{S17d})$$

114 Here, $k_v = \omega/c\beta$, $\kappa_\rho = \omega/c\beta\gamma$, and $\alpha = e^2/4\pi\epsilon_0 \hbar c$.

115 IV. MAXIMUM OF SMITH–PURCELL RADIATION LIMIT

116 In Fig. 2, we discuss the limit of Smith–Purcell radiation at a given wavelength as a func-
 117 tion of electron velocity. The electron velocity at which the limit of Smith–Purcell radiation
 118 achieves maximum corresponds to the zero of its derivative to velocity. In Eq. (4), since the
 119 integrand $\kappa_\rho^4 K_0^2(\kappa_\rho \rho) + \kappa_\rho^2 k_v^2 K_1^2(\kappa_\rho \rho)$ is continuous and differentiable, based on the Lagrange’s
 120 mean value theorem, there must exist some ρ_0 such that $\int_V \kappa_\rho^4 K_0^2(\kappa_\rho \rho) + \kappa_\rho^2 k_v^2 K_1^2(\kappa_\rho \rho) dV =$
 121 $\left[\kappa_\rho^4 K_0^2(\kappa_\rho \rho_0) + \kappa_\rho^2 k_v^2 K_1^2(\kappa_\rho \rho_0) \right] V$. Therefore,

$$\begin{aligned} \frac{d\Gamma(\omega)}{d\beta} &\propto \frac{d\Gamma(\omega)}{d\kappa_\rho} \frac{d\kappa_\rho}{d\beta} \propto \frac{d\Gamma(\omega)}{d\kappa_\rho} \\ &\propto 4\kappa_\rho^3 K_0^2(\kappa_\rho \rho_0) - (3\kappa_\rho^4 \rho_0 + \kappa_\rho^2 k^2 \rho_0) K_0(\kappa_\rho \rho_0) K_1(\kappa_\rho \rho_0) \\ &\quad + (4\kappa_\rho^3 + 2\kappa_\rho k^2) K_1^2(\kappa_\rho \rho_0) - \rho_0 \kappa_\rho^2 (\kappa_\rho^2 + k^2) K_1(\kappa_\rho \rho_0) K_2(\kappa_\rho \rho_0). \end{aligned} \quad (\text{S18})$$

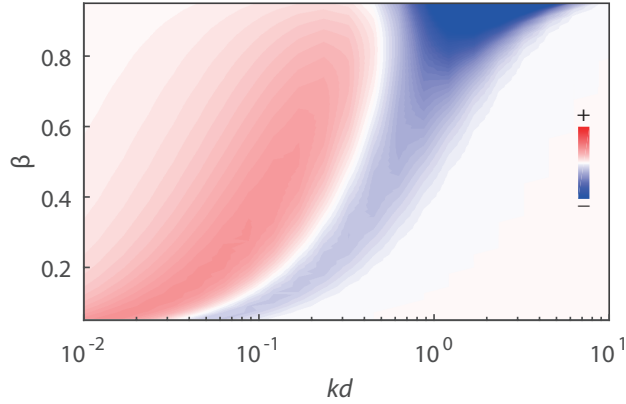


Figure S2. Plot of $\left. \frac{d^2 N(\omega)}{d\omega d\beta} \right|_{\rho_0=2d}$. There is a nodal line of zero derivative that coincides with the limit maximum in Fig. 2.

124 Fig. S2 is calculated using Eq. S18 where a nodal line of zero derivative appears and coincide
 125 with the limit maximum shown in Fig. 2(a), which is consistent with our prediction of optimal
 126 velocities as a function of kd .

127 V. LIMIT ASYMPTOTICS

128 For the asymptotic behavior of the limit, here we consider four scenarios: electrons in the near
 129 field ($kd \rightarrow 0$), electrons in the far field ($kd \rightarrow \infty$), extreme nonrealistic electrons ($v \rightarrow 0$), and

130 extreme relativistic electrons ($v \rightarrow c$). In this section we only consider the three-dimensional
 131 problem [Eq. (4)].

132 First, we consider near field $kd \rightarrow 0$. We also assume the electron speed is intermediate so
 133 neither $\beta \rightarrow 0$ (extremely slow) nor $\gamma \rightarrow \infty$ (extremely fast), which we will discuss later. In
 134 the expression of the general limit [Eq. (4)], there are two terms in the integrand where the first
 135 term (containing K_0) is the contribution from the longitudinal polarization E_x and the second term
 136 (containing K_1) is the contribution from the transverse polarization E_ρ . The hyperbolic Bessel
 137 functions K_ν in these two terms has the same argument $\kappa_\rho \rho = k\rho/\beta\gamma$, which also approaches zero
 138 for $\rho \gtrsim d$. Both $K_0(\kappa_\rho \rho)$ and $K_1(\kappa_\rho \rho)$ diverge when $\kappa_\rho \rho \rightarrow 0$ but at different divergence rates [4]:

$$139 \quad \lim_{\rho \rightarrow 0} K_0(\kappa_\rho \rho) \sim -\ln(\kappa_\rho \rho/2) - \gamma_0, \quad (\text{S19a})$$

$$140 \quad \lim_{\rho \rightarrow 0} K_1(\kappa_\rho \rho) \sim \frac{1}{\kappa_\rho \rho}, \quad (\text{S19b})$$

142 where γ_0 is the Euler–Mascheroni constant. Therefore, $K_1(\kappa_\rho \rho) \gg K_0(\kappa_\rho \rho)$ when $\kappa_\rho \rho \rightarrow 0$ and E_ρ
 143 has the major contribution to the limit.

144 Second, we consider electron beams in the far field $kd \rightarrow \infty$:

$$145 \quad \lim_{\rho \rightarrow \infty} K_0(\kappa_\rho \rho) \sim \sqrt{\frac{\pi}{2\kappa_\rho \rho}} e^{-\kappa_\rho \rho} \left[1 - \frac{1}{8\kappa_\rho \rho} + \mathcal{O}(\kappa_\rho^2 \rho^2) \right], \quad (\text{S20a})$$

$$146 \quad \lim_{\rho \rightarrow \infty} K_1(\kappa_\rho \rho) \sim \sqrt{\frac{\pi}{2\kappa_\rho \rho}} e^{-\kappa_\rho \rho} \left[1 + \frac{3}{8\kappa_\rho \rho} + \mathcal{O}(\kappa_\rho^2 \rho^2) \right]. \quad (\text{S20b})$$

148 Therefore, both E_x –limit and E_ρ –limit decay exponentially at the same rate and E_ρ –limit remains
 149 be higher.

150 Third, we consider asymptotic behavior of the limit when the electrons are extremely nonrelativistic
 151 ($\beta \rightarrow 0$). In this limit, we have $\lim_{\beta \rightarrow 0} \kappa_\rho = k_v \rightarrow \infty$. Thus in Eq. (4)

$$152 \quad \lim_{\kappa_\rho \rightarrow \infty} \kappa_\rho^2 K_0(\kappa_\rho \rho) \sim \sqrt{\frac{\pi}{2\kappa_\rho \rho}} \kappa_\rho^2 e^{-\kappa_\rho \rho} \left[1 - \frac{1}{8\kappa_\rho \rho} + \mathcal{O}(\kappa_\rho^2 \rho^2) \right] = 0, \quad (\text{S21a})$$

$$153 \quad \lim_{\kappa_\rho \rightarrow \infty} \kappa_\rho k_v K_1(\kappa_\rho \rho) \sim \sqrt{\frac{\pi}{2\kappa_\rho \rho}} \kappa_\rho^2 e^{-\kappa_\rho \rho} \left[1 + \frac{3}{8\kappa_\rho \rho} + \mathcal{O}(\kappa_\rho^2 \rho^2) \right] = 0, \quad (\text{S21b})$$

155 which is consistent with the fact that static charges do not generate radiation. Our computational
 156 verification is shown in Fig. 2(b) and (c) where both the limit and numerical results approach
 157 zero as $\beta \rightarrow 0$ for either small or large separations (whether slow or fast electrons are preferred)
 158 between the electron beams and the structure.

159 Last, we consider the limit behavior when the electrons are extremely relativistic, where
 160 $\lim_{\beta \rightarrow 1} \kappa_\rho = \sqrt{\omega^2/v^2 - \omega^2/c^2} = 0$:

$$161 \quad \lim_{\kappa_\rho \rightarrow 0} \kappa_\rho^2 K_0(\kappa_\rho \rho) \sim \kappa_\rho^2 \left[-\ln(\kappa_\rho \rho/2) - \gamma_0 \right] = 0, \quad (\text{S22a})$$

$$162 \quad \lim_{\kappa_\rho \rightarrow 0} \kappa_\rho k_v K_1(\kappa_\rho \rho) \sim \kappa_\rho k_v / \kappa_\rho \rho = k_v / \rho. \quad (\text{S22b})$$

164 Therefore, in this limit, E_x contribution vanishes but E_ρ remains finite. The entire problem be-
 165 comes equivalent to a plane-wave scattering problem since the incident field is purely transverse.

166 VI. PENETRATING ELECTRON TRAJECTORIES

167 In the main text, we discuss electron trajectories *near* photonic structures. For *penetrating*
 168 electron trajectories—that is, when the electron trajectory $\mathbf{r}_e(t)$ intersects $\chi(\mathbf{r}) \neq 0$ regions—a
 169 subtlety arises: the limit, Eq. (3), then apparently diverges even in lossy materials $\text{Im}\chi \neq 0$. In
 170 specific terms, the norm-squared incident field \mathbf{E}_{inc} is non-integrable over the electron trajectory,
 171 that is $\int_V dV |\mathbf{E}_{\text{inc}}(\mathbf{r})|^2 \sim \int_V dV |\hat{\mathbf{x}} \kappa_\rho \ln \kappa_\rho \rho + \hat{\rho} \gamma \rho^{-1}|^2$ diverges if V includes regions where $\rho = 0$.
 172 Here, we discuss the regularization of this divergence with emphasis on the implications to electron
 173 energy loss spectroscopy (EELS).

174 Though at first sight disconcerting, the divergence is not a surprise: the direct calculation of
 175 the EEL spectrum, $\Gamma(\boldsymbol{\rho}, \omega) = \frac{e^2}{\pi \hbar \omega} \text{Re} \int_{-\infty}^{\infty} dx E_x(\boldsymbol{\rho} + x \hat{\mathbf{x}}, \omega) e^{-ik_v z}$, is also divergent for penetrating
 176 trajectories when $\text{Im}\chi \neq 0$. For an extended bulk material, of permittivity $\epsilon = 1 + \chi$, the EEL
 177 spectrum (per unit length L) can be evaluated from the momentum-space representation of the
 178 total field (to be introduced shortly), yielding [2]:

$$179 \quad \Gamma_{\text{EELS}}(\omega) = \frac{e^2 L}{\pi \hbar v^2} \text{Im} \left[\left(\frac{v}{c} - \frac{1}{\epsilon} \right) \ln \left(\frac{q_c^2 + k_v^2 - \epsilon k^2}{k_v^2 - \epsilon k^2} \right) \right]. \quad (\text{S23})$$

180 The denominator of the logarithm describes the emergence of Cherenkov losses for $v > c/\epsilon$ and
 181 is finite—in contrast, the numerator, which describes EEL due to material loss, diverges logarith-
 182 mically in a momentum cut-off q_c . Of course, the divergence is merely an artifact of an idealized
 183 description of the system—several physical and practical considerations impose natural momen-
 184 tum cut-offs, e.g.:

185 **Collection angle:** The collection semi-angle of the microscope's spectrometer φ restricts momen-
 186 tum transfer collection to in-plane momenta $q_\rho < q_c$, with $\hbar q_c = m_e v \sin \varphi \simeq m_e v \varphi$. At typ-

187 ical collection semi-angles and acceleration voltages—say, $\varphi = 10$ mrad and 100 keV—this
 188 sets a cut-off at $\hbar q_c \approx 2.8 \times 10^3$ eV/c, or equivalently, a spatial spread $1/q_c \sim 1$ Å.

189 **Nonlocality:** Nonlocality effectively suppresses the dielectric response to large-momentum plane-
 190 wave components, i.e., $\epsilon(q, \omega) \rightarrow 1$ for $q \gg 1/a$ (lattice constant a). The free-electron
 191 response is quenched even earlier, at a threshold set by the Thomas–Fermi momentum.

192 **Electron spread:** The spread, ΔR , of the electron’s in-plane density imposes a cut-off $q_c \sim 1/\Delta R$.

193 To summarize; the divergence of the limit for penetrating trajectories is simply the mirror of the
 194 divergence of the direct calculation. Accordingly, the divergence’s remedy is also mirrored: the
 195 limit is regularized upon introducing a momentum cut-off in the electron’s (incident) field \mathbf{E}_{inc} .
 196 Denoting this regularized field $\mathbf{E}_{\text{inc},q_c}$, we next verify that this field is indeed regular as $\rho \rightarrow 0$.
 197 Coincidentally, this also outlines the derivation of the conventional, non-regularized field [Eq. (2)].

198 The derivation proceeds as follows: in momentum-frequency space, the electron charge density
 199 $\rho(\mathbf{r}, t) = -e\delta(\mathbf{r} - \mathbf{v}t)$ equals $\rho(\mathbf{q}, \omega) = -2\pi e\delta(\omega - \mathbf{q} \cdot \mathbf{v})$ and is accompanied by a current density
 200 $\mathbf{J}(\mathbf{q}, \omega) = -2\pi e\mathbf{v}\delta(\omega - \mathbf{q} \cdot \mathbf{v})$. Jointly with Maxwell’s equations, in the form of the wave-equation
 201 $(q^2 - \epsilon k^2)\mathbf{E}_{\text{inc}} = i\epsilon_0^{-1}(\mathbf{J}k/c - \rho\mathbf{q}/\epsilon)$, this gives the associated electric field’s (\mathbf{q}, ω) -representation:

$$202 \quad \mathbf{E}_{\text{inc}}(\mathbf{q}, \omega) = -\frac{2\pi i e}{\epsilon_0} \frac{k\mathbf{v}/c - \mathbf{q}/\epsilon}{q^2 - \epsilon k^2} \delta(\omega - \mathbf{q} \cdot \mathbf{v}). \quad (\text{S24})$$

203 An inverse transform then yields the (\mathbf{r}, ω) -representation (specializing to $\mathbf{v} = v\hat{\mathbf{x}}$ and $\epsilon = 1$):

$$204 \quad \begin{aligned} \mathbf{E}_{\text{inc},q_c}(\mathbf{r}, \omega) &= -\frac{2\pi i e}{\epsilon_0} \int_{|\mathbf{q}| < q_c} \frac{d^3\mathbf{q}}{(2\pi)^3} \frac{k\mathbf{v}/c - \mathbf{q}}{q^2 - k^2} \delta(\omega - \mathbf{v} \cdot \mathbf{q}) e^{i\mathbf{q} \cdot \mathbf{r}} \\ 205 \quad &= -\frac{i e}{\epsilon_0 v} e^{ik_v x} \int_{|\mathbf{q}_\rho| < q_c} \frac{d^2\mathbf{q}_\rho}{(2\pi)^2} \frac{(k\mathbf{v}/c - k_v)\hat{\mathbf{x}} - \mathbf{q}_\rho}{q_\rho^2 + k_v^2 - k^2} e^{i\mathbf{q}_\rho \cdot \boldsymbol{\rho}} \\ 206 \quad &= \frac{i e}{2\pi\epsilon_0 v} e^{ik_v x} \left[\underbrace{\frac{k_v}{\gamma^2} \int_0^{q_c} dq_\rho \frac{q_\rho J_0(q_\rho \rho)}{q_\rho^2 + k_v^2 - k^2}}_{\triangleq L_{q_c} \rightarrow \kappa_\rho K_0(\kappa_\rho \rho)/\gamma \text{ for } q_c \rightarrow \infty} \hat{\mathbf{x}} + i \underbrace{\int_0^{q_c} dq_\rho \frac{q_\rho^2 J_1(q_\rho \rho)}{q_\rho^2 + k_v^2 - k^2}}_{\triangleq T_{q_c} \rightarrow \kappa_\rho K_1(\kappa_\rho \rho) \text{ for } q_c \rightarrow \infty} \hat{\boldsymbol{\rho}} \right], \quad (\text{S25}) \end{aligned}$$

208 reproducing Eq. (2) as $q_c \rightarrow \infty$ (we remind that $\kappa_\rho \triangleq k_v/\gamma$). Written in terms of the transverse and
 209 longitudinal parts introduced in the above, L_{q_c} and T_{q_c} , the regularized version of Eq. (3) reads

$$210 \quad P_\tau(\omega) \leq \frac{e^2 \omega \xi_\tau}{16\pi^3 \epsilon_0 v^2} \int dV \frac{|\chi|^2}{\text{Im}\chi} (L_{q_c}^2 + T_{q_c}^2). \quad (\text{S26})$$

211 To demonstrate the limits’ finiteness, we require the small- ρ behavior of L_{q_c} and T_{q_c} at finite q_c .

212 Since q_c is large, much larger than κ_ρ , this is straightforward—particularly for T_{q_c} :

$$\begin{aligned}
213 \quad T_{q_c} &\triangleq \int_0^{q_c} dq_\rho \frac{q_\rho^2 J_1(q_\rho \rho)}{q_\rho^2 + \kappa_\rho^2} = \int_0^\infty dq_\rho \frac{q_\rho^2 J_1(q_\rho \rho)}{q_\rho^2 + \kappa_\rho^2} - \int_{q_c}^\infty dq_\rho \frac{q_\rho^2 J_1(q_\rho \rho)}{q_\rho^2 + \kappa_\rho^2} \\
214 \quad &\simeq \kappa_\rho K_1(\kappa_\rho \rho) - \int_{q_c}^\infty dq_\rho J_1(q_\rho \rho) = \kappa_\rho K_1(\kappa_\rho \rho) - \frac{J_0(q_c \rho)}{\rho}. \quad (\text{S27})
\end{aligned}$$

216 The small- ρ behavior then follows from the small-argument asymptotics of the Bessel functions
217 [for $x \ll 1$, $K_1(x) = x^{-1} - \frac{1}{2}x(\frac{1}{2} - \gamma_{\text{EM}} - \ln \frac{1}{2}x) + \mathcal{O}(x^3 \ln x)$ and $x^{-1}J_0(x) = x^{-1} - \frac{1}{4}x + \mathcal{O}(x^3)$ with
218 γ_{EM} denoting the Euler–Mascheroni constant]:

$$219 \quad T_{q_c} \simeq \frac{1}{2}q_c^2 \rho + \frac{1}{2}\kappa_\rho^2(\gamma_{\text{EM}} - \frac{1}{2})\rho + \frac{1}{2}\kappa_\rho^2 \ln\left(\frac{1}{2}\kappa_\rho \rho\right)\rho, \quad \text{for } \rho \ll q_c^{-1} \ll \kappa_\rho^{-1}. \quad (\text{S28})$$

220 Thus, the regularized transverse component T_{q_c} vanishes as $\rho \rightarrow 0$ —for slightly larger ρ -values,
221 however, T_{q_c} has a global maximum: $\max_{q_c \rho} T_{q_c} \approx T_{q_c}(q_c \rho \approx 2.76) \approx 0.42q_c$ (assuming $q_c \gg \kappa_\rho$).

222 The longitudinal contribution L_{q_c} does not find as neat a closed form expression as Eq. (S27),
223 though it may still be expressed in terms of known functions:

$$\begin{aligned}
224 \quad L_{q_c} &\triangleq \frac{\kappa_\rho}{\gamma} \int_0^{q_c} dq_\rho \frac{q_\rho J_0(q_\rho \rho)}{q_\rho^2 + \kappa_\rho^2} \simeq \frac{\kappa_\rho}{\gamma} \left[\int_0^\infty dq_\rho \frac{q_\rho J_0(q_\rho \rho)}{q_\rho^2 + \kappa_\rho^2} - \int_{q_c}^\infty dq_\rho \frac{J_0(q_\rho \rho)}{q_\rho} \right] \\
225 \quad &= \frac{\kappa_\rho}{\gamma} \left\{ K_0(\kappa_\rho \rho) + \ln \frac{1}{2}q_c \rho + \gamma_{\text{EM}} - \frac{1}{2}\left(\frac{1}{2}q_c \rho\right)^2 {}_2F_3 \left[\begin{matrix} 1, 1 \\ 2, 2, 2 \end{matrix} \middle| -\left(\frac{1}{2}q_c \rho\right)^2 \right] \right\}, \quad (\text{S29})
\end{aligned}$$

227 where ${}_2F_3$ is a generalized hypergeometric function with the asymptotic behavior $= 1 - \mathcal{O}[(q_c \rho)^2]$.

228 The small- ρ behavior again follows from the Bessel function asymptotics [$K_0(x) = -\ln \frac{1}{2}x - \gamma_{\text{EM}} +$
229 $\mathcal{O}(x^2 \ln x)$], such that:

$$230 \quad L_{q_c} \simeq \frac{\kappa_\rho}{\gamma} \ln \frac{q_c}{\kappa_\rho}, \quad \text{for } \rho \ll q_c^{-1} \ll \kappa_\rho^{-1}. \quad (\text{S30})$$

231 Thus, the longitudinal contribution L_{q_c} tends to a finite, nonzero value $\propto \ln q_c/\kappa_\rho$ as $\rho \rightarrow 0$; this is
232 also the maximum of L_{q_c} .

233 Equations (S28) and (S30) demonstrate that the $\rho = 0$ singularity of the incident field is regu-
234 larized for finite cut-off momenta q_c . This ensures that both direct calculations and limits similarly
235 yield finite, regularized values, with bulk contributions dependent on the cut-off momentum.

236 VII. EXPERIMENTAL METHODS AND DATA ANALYSIS

237 We are able to obtain the *absolute* intensity of Smith–Purcell radiation by implementing a cal-
238 ibration measurement using a broadband (visible and near infrared) calibrated source (AvaLight-
239 HAL-CAL). The experimental setup for calibration is shown in Fig. S3. All the optics remain the

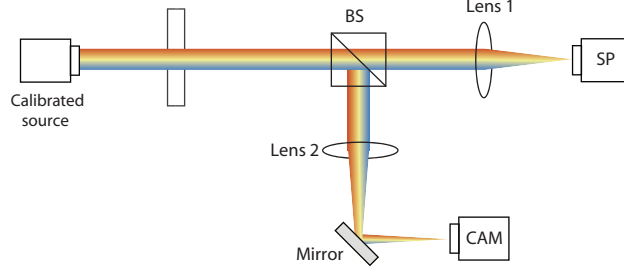


Figure S3. Experimental setup of the calibration measurement.

240 same as Fig. 3(a) except that we replace the SEM with the calibration source. The spectral inten-
 241 sity $S_0(\omega)$ of the calibrated source is already known from the manufacturer. Passing through all
 242 the optics, the radiation from the calibrated source enters the spectrometer and generates a signal
 243 count $C_0(\omega)$.

244 With $S_0(\omega)$ and $C_0(\omega)$, we are able to gauge Smith–Purcell radiation intensity $S(\omega)$ by reading
 245 the corresponding signal count $C(\omega)$. The relation is given by

$$246 \quad \frac{S_0(\omega)}{C_0(\omega)} = \frac{S(\omega)}{C(\omega)}. \quad (\text{S31})$$

247 This relation is valid for two reasons. First, the generated photons into the sample substrate is
 248 negligibly small compared to the total radiation (see Fig. S4). Second, the optics and spectrom-
 249 eter configurations remain unchanged for Smith–Purcell radiation measurement and calibration
 250 measurement. This approach allows us to obtain the absolute radiation intensity of the collected
 251 Smith–Purcell radiation, without knowing the loss functions of each individual optical elements
 252 or the quantum efficiencies and EM gains of the spectrometer at each wavelength, since all these
 253 factors will cancel out if inserted into Eq. (S31).

254 To calculate the number of photons generated per electron, measurement of the current from
 255 the SEM is necessary. The currents are measured using a picoammeter connected to a built-in
 256 Faraday cup inside the SEM chamber. The measured currents are shown in Fig. S5(a).

257 For comparisons with the analytical limits, we also need to evaluate the number of unit cells
 258 N_{uc} of interaction and consider the beam diameters (spatial spread) of the electron beams. We
 259 estimate the electron beam diameter D with the equation [7]

$$261 \quad D^2 = D_0^2 + D_d^2 + D_s^2 + D_c^2 = [C_0^2 + (0.6\lambda)^2]\alpha_p^{-2} + \frac{C_s^2\alpha_p^6}{4} + \left(C_c \frac{\Delta E}{E}\right)^2 \alpha_p^2. \quad (\text{S32})$$

262 Here D_0 is the aberration-free Gaussian probe diameter, D_d corresponds to aperture diffraction,
 263 D_s corresponds to spherical aberration, and D_c corresponds to chromatic aberration. Our SEM

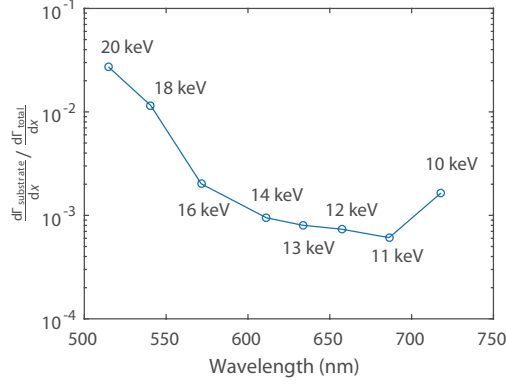


Figure S4. Fraction of the generated photons into the substrate for different accelerating voltages at normal emission angle ($\lambda = a/\beta$).

264 uses a tungsten thermionic cathode, for the voltage regime (10–20 keV) we use, D_d and D_c are
 265 negligible [8]

$$266 \quad D^2 \approx D_0^2 + D_s^2 = C_0^2 \alpha_p^{-2} + \frac{C_s^2 \alpha_p^6}{4}, \quad (S33)$$

267 where

$$268 \quad C_0 = \sqrt{4I/b\pi^2}, \quad (S34)$$

269 b is the electron gun brightness, I is the probe current, α_p is the convergence semi-angle of the
 270 electron beam, and C_s is the spherical aberration coefficient. For the brightness b of the source,
 271 we choose 1×10^5 A/cm²/sr for the acceleration voltage 20 keV (typical value for a tungsten
 272 source [7–9]) and scale it linearly [7–9] for other voltages. The focal length (working distance) of
 273 our SEM is 28 mm, which corresponds to a spherical aberration coefficient $C_s \approx 300$ mm [8, 9].

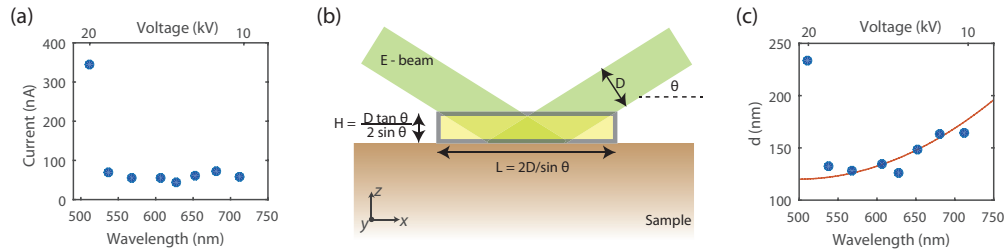


Figure S5. (a) Measured current of the experiment. (b) Schematic of the model to evaluate the interaction length of the electron beam with the structure. (c) Electron structure separations d obtained from the model (dots) and their polynomial fitting (curve; the 20 kV outlier data point dropped from fitting) for calculating theoretical upper limits.

274 For each measurement, we adjusted the SEM to achieve the smallest possible beam diameter.
 275 In theory, this corresponds to $D_{\min} = (4/3)^{3/8}(C_0^3 C_s)^{1/4}$ for the optimal convergence semi-angle
 276 $\alpha_{\text{opt}} = (4/3)^{1/8}(C_0/C_s)^{1/4}$ [derived from Eq. (S33)].

277 In our experiment, the electron beams grazingly impinges onto the sample at a nonzero angle
 278 of $\theta = 1.5^\circ$, which leads to a finite number of unit cells where electrons strongly interact with the
 279 structure such that the radiation contribution from other areas are negligible. The backscattering
 280 coefficient η of the SEM can be generally estimated as [7]

$$281 \quad \eta = 1/(1 + \sin \theta)^p, \quad (\text{S35})$$

282 where $p = 9/\sqrt{Z}$ and Z is the atomic number. In our case, $\theta = 1.5^\circ$ and $Z = 79$ (Au), and
 283 thus $\eta \approx 0.974$, meaning that most electrons get elastically scattered and maintain their initial
 284 momenta, which correspond to the scenario shown in Fig. S5(b). The highlighted rectangle is
 285 treated as the region where electrons strongly interact with the structure. The number of unit
 286 cells is consequently determined via the length of the interaction region $N_{\text{uc}} = L/a = 2D/a \sin \theta$.
 287 After obtaining N_{uc} , the measured radiation spectral density $S(\omega)$ can be translated into emission
 288 probability per electron per frequency per unit propagation length

$$289 \quad \frac{d\Gamma_{\text{expt}}(\omega)}{dx} = \frac{eS(\omega)}{\hbar\omega I N_{\text{uc}} a}, \quad (\text{S36})$$

290 which produces the measured emission probability shown in Fig. 3(d).

291 On the theory side, the upper limit in Fig. 3(d) is calculated for Smith–Purcell radiation at
 292 the surface-normal emission angle (i.e., $\beta = a/\lambda$). The limit is evaluated at the center of the
 293 interaction region with separation $d = H/2 = D \tan \theta/4 \sin \theta$ [see Fig. S5(c)] by generalizing
 294 Eq. (6). The generalization of Eq. (6), analogous to the expression of Eq. (4), is straightforward
 295 for the inhomogeneous Au-Si grating sample: move $|\chi|^2/\text{Im}\chi$ into the integrand, and account for
 296 different materials:

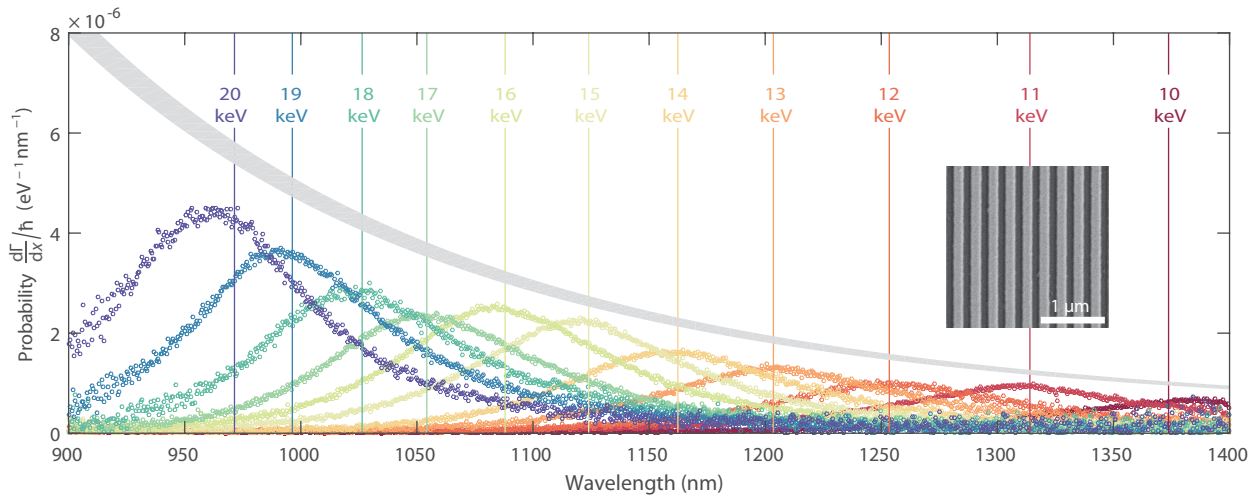
$$297 \quad \Gamma_{\tau}(\omega) \leq \frac{\alpha_{\xi\tau}^c}{2\pi\omega^2} \left\{ \int_{V_{\text{Au}}} \frac{|\chi_{\text{Au}}|^2}{\text{Im}\chi_{\text{Au}}} \left[\kappa_{\rho}^4 K_0^2(\kappa_{\rho}\rho) + \kappa_{\rho}^2 k_v^2 K_1^2(\kappa_{\rho}\rho) \right] dV + \int_{V_{\text{Si}}} \frac{|\chi_{\text{Si}}|^2}{\text{Im}\chi_{\text{Si}}} \left[\kappa_{\rho}^4 K_0^2(\kappa_{\rho}\rho) + \kappa_{\rho}^2 k_v^2 K_1^2(\kappa_{\rho}\rho) \right] dV \right\}, \quad (\text{S37})$$

299 where V_{mat} and χ_{mat} are the occupied volume and susceptibilities of the materials ($\text{mat} \in \{\text{Si}, \text{Au}\}$).

300 **VIII. NEAR-INFRARED SMITH-PURCELL RADIATION EXPERIMENT**

301 We also conduct near-infrared experiment to further confirm out theory with the same experi-
 302 mental setup and a near-infrared spectrometer. A one-dimensional grating (Au-covered patterned-
 303 Si, see Fig. S6 inset; LightSmyth Technologies) with a longer periodicity (≈ 272 nm) is used such
 304 that the Smith-Purcell radiation moves to near-infrared.

305 Adopting the same methods of data acquisition, calibration, and analysis [as those of our initial
 306 experiment in the visible (as described in Supplementary VII)], we are able to obtain the absolute
 307 emission probabilities for the near-infrared Smith-Purcell radiation. The new experimental results
 308 are shown in Fig. S6, where the envelope lineshape of the emission spectra again follows our
 309 theoretical prediction. The measured currents and the calculated electron structure separations are
 310 shown in Fig. S7.



311 Figure S6. Smith-Purcell radiation observed in the near-infrared regime and the comparison with the upper
 312 limit theory.

314 In addition to the agreement between our theory and each of the experiment, the comparison
 315 between the visible and the infrared experiment gives rise to interesting observations that further
 316 confirm our theory. Two key observations can be made from the comparison. First, the absolute
 317 emission probabilities increase by about two orders of magnitude from the visible to the near-
 318 infrared regime—consistent with the same order of increase in the material factor of Au [see
 319 Fig. 1(b)], which confirm the material factor dependence explicitly. Second, although the two
 320 experiments are both in the fast-electron-efficient regime, the measured emission probabilities
 321 feature a peak for the visible experiment, while exhibit monotonic decrease for smaller electron

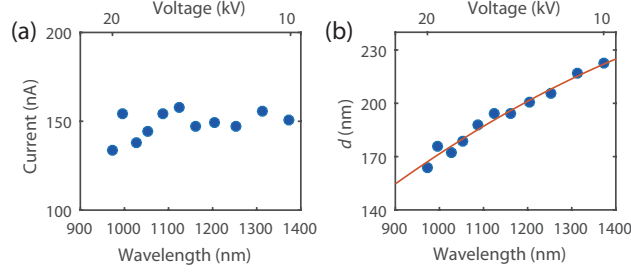


Figure S7. (a) Measured current of the near-infrared experiment. (b) Electron structure separations d obtained from the model (dots; see Supplementary VII) and their polynomial fitting (curve) for calculating theoretical upper limits.

322 energies (except for a small increase between 17 keV to 16 keV) for the near-infrared experiment.
 323 Such a difference arises because the material response is much less dispersive in the near-infrared,
 324 which implicitly corroborates the functional impact-parameter dependence within our upper limit.

325 IX. COMPLEMENTARY EVIDENCE FOR THE SLOW-ELECTRON-EFFICIENT PREDIC- 326 TION

327 In the main text, we predict that slow electrons radiate more strongly than relativistic ones
 328 at subwavelength separation ($kd \ll 1$) with structures. We also provide numerical evidence for
 329 this prediction [Fig. 2(b-c)]. In this section, we discuss a complementary supporting evidence
 330 for our slow-electron-efficient prediction based on data extracted from a recent work [10] that re-
 331 ports an integrated Cherenkov radiator using hyperbolic metamaterials (Au/SiO₂ layered stack).
 332 The electron-structure separation is reduced by integrating the electron field emitter on the chip.
 333 Ref. [10] reports the output power P_{out} of the device as a function of anode-cathode currents I_{ac} and
 334 electron energies for fixed radiation wavelengths (centered at ≈ 780 nm; see Fig. 2 in Ref. [10]).
 335 These data allow us to extract the experimental emission probabilities $\frac{d\Gamma(\omega)}{dx} \propto P_{\text{out}}/I_{\text{ac}}$, since the re-
 336 ported shapes of the radiation spectra are similar for various electron energies (i.e., almost constant
 337 emission bandwidth for various electron energies).

The probabilities are therefore shown in Fig. S8, where data reported with electron energies are shown with extra red circles. Data points without electron energies reported in [10] are interpreted as linearly-interpolated electron energies. As we explicitly show in Fig. 2, the lineshape of emission probabilities versus electron velocity contains one-to-one correspondence with kd . Hence, the

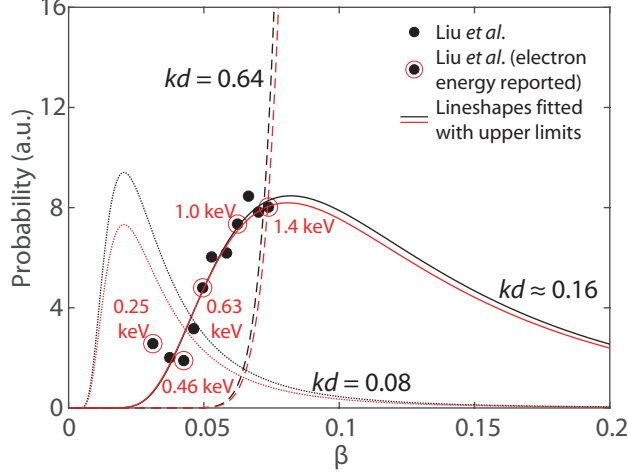


Figure S8. Extra external supporting evidence for the slow-electron-efficient prediction with small electron energies (0.25~1.4 keV), which complements our experiments using electrons with higher energies (10~20 keV). Extracted emission probabilities from [10] and the optimal lineshape fitting (solid lines with $kd \approx 0.16$) using the upper limit. The auxiliary suboptimal fittings (dashed and dotted curves) demonstrate the uniqueness of the extracted kd value. All red curves fit data points with electron energies reported, while all black curves fit all data points assuming linearly interpolated electron energies (see Fig. 2 in Ref.[10]).

experimental lineshape can be fitted with the shape-independent upper limit [Eq. (5a)] to extract the electron-structure separation d (being the only free parameter to compare with the reported value):

$$\frac{\Gamma_{\text{rad}}(\omega)}{dx} \propto \frac{|\chi_{\text{eff}}|^2}{\text{Im} \chi_{\text{eff}}} \frac{1}{\beta^2} \left[(\kappa_{\rho} d) K_0(\kappa_{\rho} d) K_1(\kappa_{\rho} d) \right], \quad (\text{S38})$$

338 where $\chi_{\text{eff}}(\chi_{\text{Au}}, \chi_{\text{SiO}_2}, \beta)$ is the effective susceptibility of the metamaterial, a function of the com-
 339 posite material permittivities and the longitudinal wavevector (i.e., the electron velocity), is ex-
 340 plicitly determined from the standard effective medium theory (see Supplementary Information
 341 of Ref. [10] S1–S3 sections). We obtain two primary fitting results in Fig. S8, where $\hat{d}_1 =$
 342 20.0 ± 2.3 nm for the solid black curve (fits all data) and $\hat{d}_2 = 19.8 \pm 6.7$ nm for the solid red
 343 curve (only fits the data with electron energies reported). The estimated $kd \approx 0.16$ corresponds to
 344 an optimal nonrelativistic electron velocity $\beta_{\text{opt}} \approx 0.08$ (see Fig. S8). We emphasize that although
 345 the only available experimental data are below the predicted β_{opt} , they are sufficient for us to unam-
 346 biguously extract the kd value for the experiment. The uniqueness of the kd value is supported by
 347 the two auxiliary suboptimal fittings (dashed and dotted curves) with either reduced or increased
 348 kd values.

349 For comparison, the reported separation from the field emitter to the structure is 40 nm. Since
 350 the electron beam in the reported device is still not theoretically ideal (not a delta function in space;
 351 instead, with nonzero beam diameters), we consider the estimates \hat{d}_1 and \hat{d}_2 , from our upper limit
 352 theory, as good agreement with the realistic structural parameter. Hence, such an agreement serves
 353 as complimentary support for our prediction about the slow-electron-efficient regime.

354 X. UPPER LIMIT IN TWO DIMENSIONS

355 The limits can be derived in both the three-dimensional or the two-dimensional case. For
 356 completeness, here we also derive the limit in the two-dimensional case, which correspond to
 357 sheet electron beams that are assumed in Fig. 4(f).

358 We consider an electron sheet beam in the (x, z) plane with charge density being one electron per
 359 nanometer, i.e., $q = 1.6 \times 10^{-19}$ C/nm [consistent with our unit for probability in two dimensions
 360 $\frac{d^2\Gamma}{dx dy}/\hbar$ (eV $^{-1}$ nm $^{-2}$)]. Precisely, the probability is invariant of the choice of the transverse (y) length
 361 scale, as long as the length scale is in the same unit for both the source current density and the
 362 probability. Here the length scale is chosen as nanometer for both of the quantities.

363 The source current density in the time domain can be written as $\mathbf{J}(\mathbf{r}, t) = qv\delta(z - z_0)\delta(x - vt)\hat{\mathbf{x}}$.
 364 In the frequency domain, the current density is given by

$$365 \quad \mathbf{J}(\mathbf{r}, \omega) = q\delta(z - z_0)e^{ik_v x}\hat{\mathbf{x}}, \quad (\text{S39})$$

366 The induced fields are

$$367 \quad \mathbf{H}(\mathbf{r}, \omega) = -\frac{q}{2}e^{ik_v x - \kappa_\rho(z - z_0)}\hat{\mathbf{y}} \quad (\text{S40a})$$

$$368 \quad \mathbf{E}(\mathbf{r}, \omega) = \frac{q}{2\omega\epsilon_0}(k_v\hat{\mathbf{z}} - i\kappa_\rho\hat{\mathbf{x}})e^{ik_v x - \kappa_\rho(z - z_0)} \quad (\text{S40b})$$

369 for $z > z_0$ and

$$371 \quad \mathbf{H}(\mathbf{r}, \omega) = \frac{q}{2}e^{ik_v x + \kappa_\rho(z - z_0)}\hat{\mathbf{y}} \quad (\text{S41a})$$

$$372 \quad \mathbf{E}(\mathbf{r}, \omega) = -\frac{q}{2\omega\epsilon_0}(k_v\hat{\mathbf{z}} + i\kappa_\rho\hat{\mathbf{x}})e^{ik_v x + \kappa_\rho(z - z_0)} \quad (\text{S41b})$$

373 for $z < z_0$, where ϵ_0 is the vacuum permittivity, and κ_ρ also defined as $\kappa_\rho = \sqrt{k_v^2 - k^2}$, same as the
 374 main text. where $k = \omega/c$ is the light wavevector.

376 Insert Eq. (S41b) into Eq. (4), we obtain the limit in two dimensions

$$377 \quad \frac{d\Gamma_\tau(\omega)}{dy} \leq \frac{|\chi|^2}{\text{Im}\chi} \frac{q^2 \xi_\tau (k_v^2 + \kappa_\rho^2)}{32\hbar\epsilon_0\omega^2} \int_S e^{-2\kappa_\rho|z - z_0|} dS, \quad (\text{S42})$$

378 where S is the area defined by the profile of the structure.

379 As in the main text, we also consider a concrete example: Smith–Purcell radiation from a
 380 rectangular grating with filling factor Λ . Applied the rectangular profile to Eq. (S42), the radiated
 381 photon per frequency per electron per unit area is bounded by

$$382 \quad \frac{d^2\Gamma_\tau(\omega)}{dx dy} \leq \frac{|\chi|^2}{\text{Im}\chi} \frac{\Lambda q^2 \xi_\tau(k_v^2 + \kappa_\rho^2)}{64\hbar\epsilon_0\kappa_\rho\omega^2} e^{-2\kappa_\rho d}, \quad (\text{S43})$$

383 where d is the distance between the electron and the grating.

384 XI. FREE ELECTRON RADIATION NEAR A BOUND STATE IN THE CONTINUUM

385 In photonic systems, modes below the light cone are guided modes, while modes above the
 386 light cone are typically resonances with finite lifetime. In contrast to guided modes or resonances,
 387 a bound state in the continuum is a perfectly confined modes with infinite lifetime embedded in
 388 the radiation continuum (above light cone) [11].

389 These properties can be used to distinguish whether an optical resonance is a BIC or not. The
 390 mode profile in Fig. 4(c) corresponds to a BIC because 1) it is obviously within the continuum
 391 [see Fig. 4(a)]; 2) it possesses infinite lifetime without external radiation (no outgoing oscillatory
 392 radiation in its eigenmode profile), as shown in Fig. S9(a).

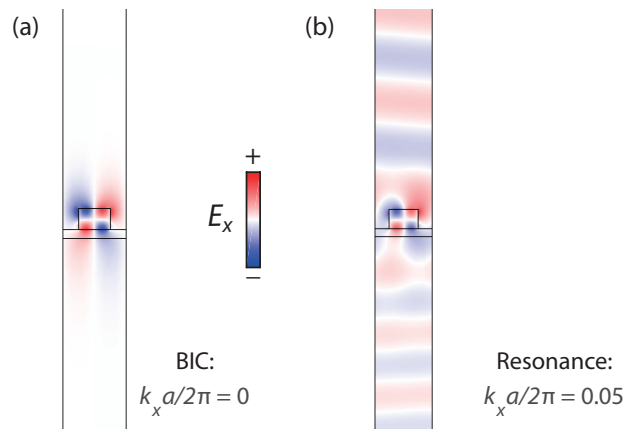


Figure S9. Difference of a BIC and a resonance on the TE₁ band of Fig. 4(a). (a) The mode profile of a BIC decays exponentially, giving rise to infinite lifetime; (b) The mode profile of a resonance contains oscillatory radiation into the far field, leading to finite lifetime.

394

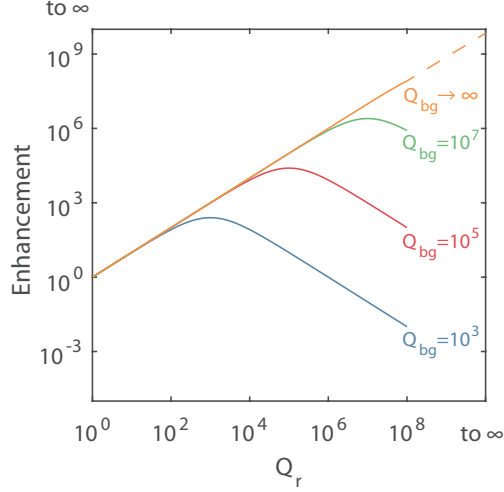


Figure S10. Smith–Purcell radiation enhancement as a function of resonant quality factors under different background quality factors.

395 Next we explain the Smith-Purcell radiation enhancement near a BIC. We write down the tem-
 396 poral coupled mode theory [12] for the coupling process

$$397 \quad \frac{da}{dt} = -i\omega_0 a - a \left(\frac{1}{\tau_{bg}} + \frac{1}{\tau_r} \right) + \sqrt{\frac{2}{\tau_r}} s_+, \quad (S44)$$

399 where a is the mode amplitude inside the resonances, $1/\tau_{bg}$ is the background coupling rate (such
 400 as material absorption and scattering loss due to fabrication impefections), $1/\tau_r$ is the resonant
 401 coupling rate (for BIC, $\tau_r = \infty$), s_+ is the wave amplitude carried by the electron towards the
 402 resonances. Solving Eq. (S44) for a we have

$$403 \quad \left| \frac{a}{s_+} \right|^2 = \frac{2/\tau_e}{(\omega - \omega_0)^2 + \left(\frac{1}{\tau_{bg}} + \frac{1}{\tau_r} \right)^2} \quad (S45)$$

405 Assuming on-resonance condition ($\omega = \omega_0$, electron line and photonic bands intersects), to maxi-
 406 mize the resonance amplitude for a given fixed s_+ , we have

$$407 \quad \left| \frac{a}{s_+} \right|^2 = \frac{2/\tau_r}{\left(\frac{1}{\tau_{bg}} + \frac{1}{\tau_r} \right)^2} \propto \frac{Q_{tot}^2}{Q_r}. \quad (S46)$$

409 where $Q = \omega\tau/2$ for all channels and $1/Q_{tot} = 1/Q_r + 1/Q_{bg}$. It is thus evident from Eq. (S46)
 410 that the maximal resonance enhancement is achieved when $Q_{bg} = Q_r$, (i.e., $\tau_{bg} = \tau_r$) which is the
 411 “Q-matching condition” we refer to in the manuscript.

412 As a result, the achievable radiation enhancement depends on the background radiation rate
413 (see Fig. S10). In our example shown in Fig. 4(f) with material absorption taken into account, the
414 maximal enhancement occurs at small offsets from the BIC with a $Q_r \approx 10^3 \sim 10^5$.

- 415 [1] A. Welters, Y. Avniel, and S. G. Johnson, *Phys. Rev. A* **90**, 023847 (2014).
416 [2] F. G. De Abajo, *Rev. Mod. Phys.* **82**, 209 (2010).
417 [3] J. D. Jackson, *Classical electrodynamics* (John Wiley & Sons, 2007).
418 [4] M. Abramowitz and I. A. Stegun, *Handbook of mathematical functions: with formulas, graphs, and*
419 *mathematical tables*, Vol. 55 (Courier Corporation, 1964).
420 [5] J. Kong, *Electromagnetic Waves Theory* (EMW Publishing, Cambridge, MA, 2005).
421 [6] C. S. Meijer, *Proc. Nederl. Akad. Wetensch.* **49**, 344 (1946).
422 [7] J. Goldstein, D. E. Newbury, D. C. Joy, C. E. Lyman, P. Echlin, E. Lifshin, L. Sawyer, and J. Michael,
423 *Scanning Electron Microscopy and X-ray Microanalysis* (Springer Science & Business Media, 2012).
424 [8] L. Reimer, *Scanning electron microscopy: physics of image formation and microanalysis*, Vol. 45
425 (Springer-Verlag, 1998).
426 [9] A. Khursheed, *Scanning electron microscope optics and spectrometers* (World scientific, 2011).
427 [10] F. Liu, L. Xiao, Y. Ye, M. Wang, K. Cui, X. Feng, W. Zhang, and Y. Huang, *Nat. Photon.* **11**, 289
428 (2017).
429 [11] C. W. Hsu, B. Zhen, A. D. Stone, J. D. Joannopoulos, and M. Soljačić, *Nat. Rev. Mater.* **1**, 16048
430 (2016).
431 [12] J. D. Joannopoulos, S. G. Johnson, J. N. Winn, and R. D. Meade, *Photonic crystals: molding the flow*
432 *of light* (Princeton university press, 2011).